Monthly Notices
of the
ROYAL ASTRONOMICAL SOCIETY

MNRAS **439,** 1245–1269 (2014) doi:10.1093/mnras/stt2391
Advance Access publication 2014 February 12

Galaxy And Mass Assembly (GAMA): *ugrizYJHK* Sérsic luminosity functions and the cosmic spectral energy distribution by Hubble type

Lee S. Kelvin,[1,2,3★] Simon P. Driver,[2,3] Aaron S. G. Robotham,[2,3] Alister W. Graham,[4] Steven Phillipps,[5] Nicola K. Agius,[6] Mehmet Alpaslan,[2,3] Ivan Baldry,[7] Steven P. Bamford,[8] Joss Bland-Hawthorn,[9] Sarah Brough,[10] Michael J. I. Brown,[11] Matthew Colless,[12] Christopher J. Conselice,[8] Andrew M. Hopkins,[10] Jochen Liske,[13] Jon Loveday,[14] Peder Norberg,[15] Kevin A. Pimbblet,[11,16,17] Cristina C. Popescu,[6] Matthew Prescott,[18] Edward N. Taylor[19] and Richard J. Tuffs[20]

[1]*Institut für Astro- und Teilchenphysik, Universität Innsbruck, Technikerstraße 25, A-6020 Innsbruck, Austria*
[2]*School of Physics and Astronomy, University of St Andrews, North Haugh, St Andrews, Fife KY16 9SS, UK*
[3]*International Centre for Radio Astronomy Research, 7 Fairway, The University of Western Australia, Crawley, Perth, Western Australia 6009, Australia*
[4]*Centre for Astrophysics and Supercomputing, Swinburne University of Technology, Hawthorn, Victoria 3122, Australia*
[5]*Astrophysics Group, H. H. Wills Physics Laboratory, University of Bristol, Tyndall Avenue, Bristol BS8 1TL, UK*
[6]*Jeremiah Horrocks Institute, University of Central Lancashire, Preston PR1 2HE, UK*
[7]*Astrophysics Research Institute, Liverpool John Moores University, Twelve Quays House, Egerton Wharf, Birkenhead CH41 1LD, UK*
[8]*School of Physics and Astronomy, The University of Nottingham, University Park, Nottingham NG7 2RD, UK*
[9]*Sydney Institute for Astronomy, School of Physics A28, University of Sydney, NSW 2006, Australia*
[10]*Australian Astronomical Observatory, PO Box 915, North Ryde, NSW 1670, Australia*
[11]*School of Physics, Monash University, Clayton, VIC 3800, Australia*
[12]*Research School of Astronomy and Astrophysics, The Australian National University, Canberra, ACT 2611, Australia*
[13]*European Southern Observatory, Karl-Schwarzschild-Str. 2, D-85748 Garching, Germany*
[14]*Astronomy Centre, University of Sussex, Falmer, Brighton BN1 9QH, UK*
[15]*Institute for Computational Cosmology, Department of Physics, Durham University, South Road, Durham DH1 3LE, UK*
[16]*Department of Physics, University of Oxford, Denys Wilkinson Building, Keble Road, Oxford OX1 3RH, UK*
[17]*Department of Physics and Mathematics, University of Hull, Cottingham Road, Hull HU6 7RX, UK*
[18]*Astrophysics Group, Department of Physics, University of the Western Cape, 7535 Bellville, Cape Town, South Africa*
[19]*School of Physics, the University of Melbourne, Parkville, VIC 3010, Australia*
[20]*Max Planck Institut für Kernphysik, Saupfercheckweg 1, D-69117 Heidelberg, Germany*

Accepted 2013 December 9. Received 2013 December 9; in original form 2013 October 11

ABSTRACT

We report the morphological classification of 3727 galaxies from the Galaxy and Mass Assembly survey with $M_r < -17.4$ mag and in the redshift range $0.025 < z < 0.06$ (2.1×10^5 Mpc^3) into E, S0-Sa, SB0-SBa, Sab-Scd, SBab-SBcd, Sd-Irr and little blue spheroid classes. Approximately 70 per cent of galaxies in our sample are disc-dominated systems, with the remaining ∼30 per cent spheroid dominated. We establish the robustness of our classifications, and use them to derive morphological-type luminosity functions and luminosity densities in the *ugrizYJHK* passbands, improving on prior studies that split by global colour or light profile shape alone. We find that the total galaxy luminosity function is best described by a double-Schechter function while the constituent morphological-type luminosity functions are well described by a single-Schechter function. These data are also used to derive the star formation rate densities for each Hubble class, and the attenuated and unattenuated (corrected for dust) cosmic spectral energy distributions, i.e. the instantaneous energy production budget. While the observed optical/near-IR energy budget is dominated 58:42 by galaxies with a significant spheroidal component, the actual energy production rate is

★ E-mail: lee.kelvin@uibk.ac.at

reversed, i.e. the combined disc-dominated populations generate ∼1.3 times as much energy as the spheroid-dominated populations. On the grandest scale, this implies that chemical evolution in the local Universe is currently largely confined to mid-type spiral classes like our Milky Way.

Key words: galaxies: elliptical and lenticular, cD – galaxies: fundamental parameters – galaxies: luminosity function, mass function – galaxies: spiral.

1 INTRODUCTION

In his seminal 1926 paper 'Extra-galactic Nebulae', Edwin Hubble established a framework for the morphological classification of galaxies which remains in use essentially unchanged to the present day. From a sample of 400 galaxies, and perhaps drawing inspiration from Jeans (1919) and Reynolds (1920), Hubble defined three main sub-groups: elliptical, spiral and lenticular (Hubble 1926, 1936). Elliptical early-type galaxies typically show no additional structure beyond a smooth radial light profile. Conversely, late-type spiral galaxies consist of a central spheroidal bulge surrounded by a flattened extended disc containing spiral arm features, and perhaps with the presence of a bar. Lenticular galaxies fall somewhere in between, with the familiar late-type bulge and disc features present, potentially with the addition of a bar, and yet the noticeable absence of spiral arm structure.

Many additions have been suggested to Hubble's classification scheme, in order to account for, e.g. the presence of rings (Sandage 1961); transition lenticular galaxies (Holmberg 1958); bulge-less Sd-type disc galaxies (Shapley & Paraskevopoulos 1940); the 'boxy' and 'discy' isophotes of early-type galaxies (Carter 1978, 1987; Davies et al. 1983; Kormendy & Bender 1996); the large variation in lenticular bulge-to-disc ratios (van den Bergh 1976; Laurikainen et al. 2010; Cappellari et al. 2011; Kormendy & Bender 2012); and the presence of dwarf galaxies (Shapley 1938; Sandage & Binggeli 1984). These additions each provide important information to morphological classification schemes, adding additional resolution to each classification element.

Moreover, while morphology is intrinsically linked to the star formation rate (SFR) of the galaxy, it was shown by Dressler (1980) that the distribution of morphological types varies as a function of the local galaxy density: the morphology–density relation. Many possible explanations for this exist in the literature, including four key effects: strangulation (Larson, Tinsley & Caldwell 1980; Kauffmann, White & Guiderdoni 1993; Diaferio et al. 2001), harassment (Moore et al. 1996), ram pressure stripping (Gunn & Gott 1972) and minor merging or tidal interactions (Park, Gott & Choi 2008). Each of these mechanisms in some way affects the SFR of the interacting system, shutting off star formation for galaxies in overdense regions and consequently causing a change in colour and ultimately morphology. Possibly more fundamental than the relation between morphology and environment is the connection between galaxy structure (i.e. bulge, disc, bar) and its host galaxy's stellar mass (van der Wel 2008; Bamford et al. 2009; Nair & Abraham 2010; Pimbblet & Jensen 2012; Wilman & Erwin 2012).

The logical basis for defining these morphological groupings remains a visual one, and so becomes increasingly time consuming in an era of large-scale observational astronomy. Despite this, the scientific worth of morphological classification remains extremely high. The morphological class of a galaxy is a tracer of its evolutionary history, with merging events believed to be the primary cause of the transition of late-type spirals into early-type ellipticals (e.g. Park et al. 2008).

In this paper, we provide morphological classifications for a local ($0.025 < z < 0.06$) volume-limited sample of 3727 galaxies brighter than $M_{r,\mathrm{Sérsic}} = -17.4$ mag taken from the Galaxy and Mass Assembly (GAMA) survey (Driver et al. 2009). Using these classifications, we measure the global and constituent morphological-type luminosity functions (MLFs) in optical *ugriz*[1] and near-infrared *YJHK*[2] passbands.

This paper is structured as follows. We define our sample and postage-stamp cutout creation in Section 2. This sample is morphologically classified by eye by three independent observers, described in Section 3. We explore the trends with morphology against complementary global galaxy measurements such as colour, stellar mass and Sérsic index in Section 4. We present the global and the individual MLFs for all nine passbands in Section 5, and discuss the division of the cosmic spectral energy distribution (CSED) by morphology, both with and without suitable corrections to account for dust attenuation, in Section 6. A standard cosmology of $(H_0, \Omega_\mathrm{m}, \Omega_\Lambda) = (70\ \mathrm{km\ s^{-1}\ Mpc^{-1}}, 0.3, 0.7)$ is assumed throughout this paper.

2 DATA

Our data are taken from the GAMA survey (Driver et al. 2009, 2011), specifically GAMA phase 1, known as GAMA-I. GAMA is a combined spectroscopic and multiwavelength imaging programme designed to study the spatial structure in the nearby ($z < 0.25$) Universe on kpc to Mpc scales (see Driver et al. 2009 for an overview). The survey, after completion of phase 1, consists of three regions of sky each of 4° (Dec.) × 12° (RA), close to the equatorial region, at approximately 9^h (135°; G09), 12^h (180°; G12) and $14^\mathrm{h}.5$ (217°.5; G15). The three regions were selected to enable accurate characterization of the large-scale structure over a range of redshifts and with regard to practical observing considerations and constraints. They lie within areas of sky surveyed by both the Sloan Digital Sky Survey (SDSS; York et al. 2000; Abazajian et al. 2009) as part of its Main Survey, and by the United Kingdom Infrared Telescope (UKIRT) as part of the UKIRT Infrared Deep Sky Survey (UKIDSS) Large Area Survey (UKIDSS-LAS; Lawrence et al. 2007). These data provide moderate depth and resolution imaging in *ugrizYJHK* suitable for analysis of nearby galaxies. GAMA imaging data presented in this paper are constructed from reprocessed SDSS and UKIDSS-LAS imaging data, rescaled to a common pixel scale of 0.339 arcsec pixel^{-1} and to a common zero-point magnitude of 30 mag arcsec^{-2}. Further details on the GAMA imaging pipeline may be found in Hill et al. (2011). The accompanying spectroscopic input catalogue was derived from the SDSS PHOTO parameter (Stoughton et al. 2002) as described in Baldry et al. (2010). The GAMA spectroscopic programme (Robotham et al.

[1] These passbands have effective wavelength mid-points of 354, 475, 622, 763 and 905 nm, respectively.

[2] These passbands have effective wavelength mid-points of 1031, 1248, 1631 and 2201 nm, respectively.

2010) commenced in 2008 using 2dF+AAOmega on the Anglo-Australian Telescope to obtain distance information (redshifts) for all galaxies brighter than $r < 19.8$ mag. The survey is ∼99 per cent complete to $r < 19.4$ mag in G09 and G15 and $r < 19.8$ mag in G12, with a median redshift of $z \sim 0.2$. Full details of the GAMA-I spectroscopic programme, key survey diagnostics, and the GAMA public and team data bases are given in Driver et al. (2011) and Hopkins et al. (2013).

2.1 Luminosity limits

2.1.1 Absolute Sérsic magnitudes

Although the GAMA survey limits mentioned above are defined using SDSS Petrosian photometry, our preferred measures of total magnitudes are those derived from truncated single-Sérsic fits to the data (see Kelvin et al. 2012). Initially a generalization of the de Vaucouleurs (1948) $r^{1/4}$ model for describing the radial light profiles of early-type galaxies, the Sérsic (1963, 1968) $r^{1/n}$ model, subsequently reviewed in Graham & Driver (2005), has become a standard tool for quantifying galaxies across a wide range of morphologies, both early and late type. The Sérsic equation provides the intensity I at a given radius r as given by

$$I(r) = I_{\rm e} \exp\left[-b_n\left(\left(\frac{r}{r_{\rm e}}\right)^{1/n} - 1\right)\right], \quad (1)$$

where $I_{\rm e}$ is the intensity at the effective radius $r_{\rm e}$, the radius containing half of the projected total light, and n is the Sérsic index which determines the shape of the light profile. The value of b_n is a function of Sérsic index, as defined in Ciotti (1991), and is such that $\Gamma(2n) = 2\gamma(2n, b_n)$, where Γ and γ represent the complete and incomplete gamma functions respectively.[3] Single-Sérsic model fits have been shown to provide a good description of galaxy light profiles as faint as $B \sim 28$ mag arcsec^{-2} (Caon, Capaccioli & Rampazzo 1990; Caon, Capaccioli & D'Onofrio 1993, 1994). Therefore, Sérsic modelling allows us to account for the missing flux in the wings of high central concentration galaxies, side stepping the well-documented problems with both Petrosian and Kron photometry (see, e.g., Graham & Driver 2005; Graham et al. 2005). We elect to truncate our Sérsic magnitudes at 10 multiples of the half-light radius (10 $r_{\rm e}$). This is to avoid extrapolation of flux into regimes below the limiting isophote for which we are uncertain of the true light profile of the galaxy: consequently not parametrizing our ignorance. For further discussion of Sérsic photometry and truncation, see Kelvin et al. (2012).

For a given band x, absolute Sérsic magnitudes M_x are derived using the standard relation

$$M_x = m_x - \left(5\log_{10} D_{\rm L} + 25\right) - k_x - e_x - A_x, \quad (2)$$

where m_x denotes the apparent magnitude (in this case, truncated Sérsic), $D_{\rm L}$ is the luminosity distance of the galaxy in megaparsecs [where $D_{\rm L}$ is related to the angular diameter distance, $D_{\rm A}$, using the relation $D_{\rm L} = (1+z)^2 D_{\rm A}$], k_x is the applied k-correction for band x, e_x is the evolutionary correction and A_x is the Milky Way dust attenuation correction. We obtain appropriate k-corrections from version 8 of the GAMA-I stellar masses catalogue (StellarMassesv08; see Taylor et al. 2011). One would expect minimal evolutionary effects over the narrow redshift range of this sample (see, e.g., Prescott, Baldry & James 2009), and so we do not apply any e-corrections to these data. We apply the Milky Way dust attenuation correction as given in table 22 of Stoughton et al. (2002), with UKIDSS values determined by matching UKIDSS data base values from the UKIRT Wide Field Camera (WFCAM) Science Archive to the SDSS extinction in the r band. Further details on this procedure may be found in Liske et al. (in preparation).

[3] b_n can trivially be calculated using the programming language R using the relation $b_n = {\rm qgamma}(0.5, 2n)$, where qgamma is the quantile function for the Gamma distribution. For the range $0.5 < n < 10$, Capaccioli (1989) approximates the value of b_n using the relation $b_n = 1.9992n - 0.3271$.

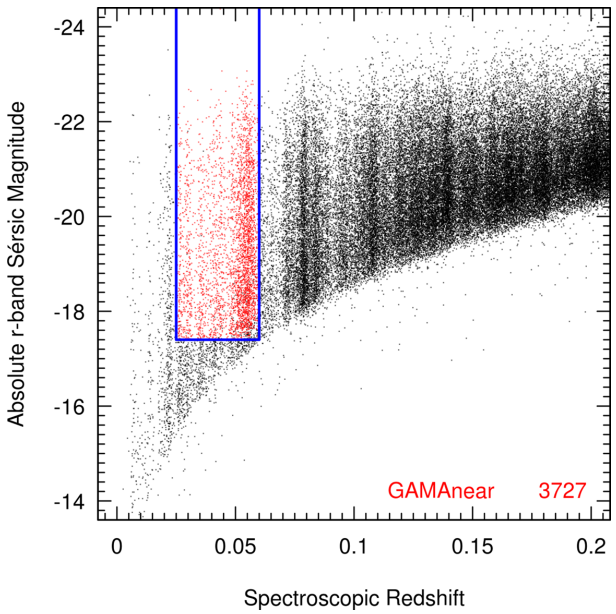

Figure 1. Absolute Sérsic magnitude (r band) as a function of local flow-corrected spectroscopic redshift for galaxies within the GAMA survey. Red data points inside the blue box represent the 3727 galaxies in the GAMAnear sample. Local flow-corrected spectroscopic redshifts are taken from version 7 of the local flow-corrected redshift catalogue (DistancesFramesv07), and absolute Sérsic magnitudes from version 7 of the Sérsic photometry catalogue (SersicCatAllv07; Kelvin et al. 2012).

2.1.2 Absolute Sérsic magnitude limit in the r band

In order to avoid the many incompleteness issues affecting the dwarf systems (both Malmquist and surface-brightness bias), in this study we focus on the more luminous systems by removing those galaxies with an absolute Sérsic magnitude in the r band fainter than $M_r = -17.4$ mag. This value is determined based on the faintest magnitude down to which our GAMA sample would be complete at our upper redshift limit of $z = 0.06$ ($m_r \sim 19.4$ mag; see Appendix A and Fig. 1). Sérsic and structural measurements are taken from version 7 of the GAMA-I Sérsic photometry catalogue (SersicPhotometryv07; Kelvin et al. 2012). To summarize this study: a two-dimensional single-Sérsic model is fitted to each galaxy in our sample using the SIGMA galaxy fitting pipeline. SIGMA is a wrapper around several contemporary commonplace astronomy tools including Source Extractor (Bertin & Arnouts 1996), PSF Extractor (Bertin 2011) and GALFIT (Peng et al. 2010).

2.2 Sample definition

Using the latest version (version 16) of the GAMA-I tiling catalogue[4] (TilingCatv16; see Baldry et al. 2010), we define a

[4] All GAMA catalogues are available through the GAMA data base, available online at http://www.gama-survey.org/.

Table 1. A summary of the GAMA data products that have been collated for this study. GAMA catalogues and their associated data products are grouped into Data Management Units (DMUs), which are also listed here for reference.

DMU	Version	Catalogue	Paper	Summary of data products used in this study
InputCat	16	TilingCat	Baldry et al. (2010)	Target information (RA, Dec., SDSS Petrosian magnitude, survey class)
InputCat	16	InputCatA	Baldry et al. (2010)	Extinction corrections
LocalFlowCorrection	7	DistancesFrames	Baldry et al. (2012)	Local flow-corrected spectroscopic redshifts, redshift quality flags
StellarMasses	8	StellarMasses	Taylor et al. (2011)	Global galaxy colours, *k*-corrections (private communication)
SersicPhotometry	7	SersicCatAll	Kelvin et al. (2012)	Sérsic photometry, structural measurements

volume-limited sample of 3727 galaxy-like (SURVEY_CLASS $\geq$ 2) objects whose local flow-corrected redshifts z lie in the range $0.025 < z < 0.06$ (see Appendix A) with an associated normalized redshift quality $nQ > 2$ (i.e. good for science[5]), an extinction-corrected r-band SDSS Petrosian magnitude of $r < 19.4$ mag (ensuring a consistent depth across all three GAMA regions) and an absolute truncated Sérsic magnitude in the r band of $M_r < -17.4$ mag. This luminosity- and volume-limited sample of 3727 galaxies is referred to as GAMAnear.

Our redshift limits give this sample a volume of 2.1×10^5 Mpc^3. Note that redshifts have been matched from version 7 of the local flow-corrected redshift catalogue (DistancesFramesv07), itself based on data from version 8 of the GAMA-I spectroscopic catalogue (SpecObjv08). These redshifts are Milky Way centric, but local velocity field effects have been removed. Matching to the GAMA galaxy group catalogue (G3C; Robotham et al. 2011), we find that just under half (1797, ∼48 per cent) of our galaxies lie in identified groups with two or more members, with 672 galaxies (∼18 per cent) in groups with a richness greater than 5, i.e. our sample is predominantly field dominated.

Fig. 1 shows absolute Sérsic magnitude (r band) as a function of local flow-corrected spectroscopic redshift for the full GAMA data set (black points). Red data points inside the blue box represent the 3727 galaxies in the GAMAnear sample. A summary of all GAMA data products used to define these samples is shown in Table 1.

2.3 Magnitude limits in additional passbands

The r-band absolute magnitude limit for our volume-limited GAMAnear sample ($M_r = -17.4$ mag) introduces a colour-dependent limit across the remaining eight passbands in use from the SDSS and UKIDSS. This variable limit has the potential to introduce incompleteness bias when analysing data at other wavelengths, and so (following Driver et al. 2012), we define additional limits down to which the sample remains complete and unbiased as a function of colour for each passband.

The colour–magnitude diagrams in Fig. 2 show the relation between colour and absolute magnitude for galaxies in the GAMAnear sample. Long-dashed lines represent the r-band limit of $M_r = -17.4$ mag. One can clearly see the two distinct populations (i.e. a bimodal distribution in both colour and absolute magnitude) in the g-band data; the blue cloud and red sequence. These two populations are also evident to a lesser extent at all wavelengths.

We define the additional faint-end limits visually as the absolute magnitude in band x (where $x = ugizYJHK$) at which the main body of the data intersects the $M_r = -17.4$ mag line. These passband limits are listed in Table 2, and shown as vertical short-dashed lines in Fig. 2. The absolute magnitude of the Sun in all passbands is also shown in Table 2, for reference (values taken from table 1 of Hill et al. 2010).

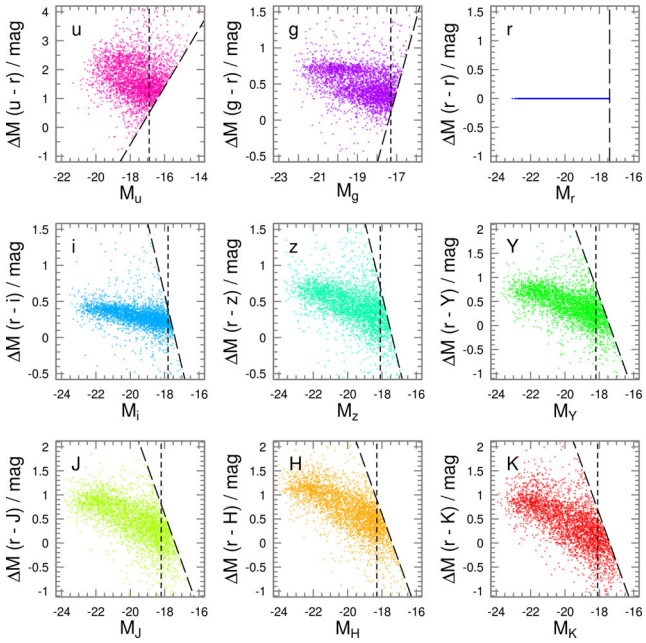

Figure 2. Colour–magnitude diagrams for all galaxies in the GAMAnear sample across all nine bands. These values are derived from absolute Sérsic magnitudes truncated at 10 r_e with k-corrections and Galactic dust corrections applied. Long-dashed lines represent the volume-limited sample limit of $M_r = -17.4$ mag. Short-dashed lines represent the absolute magnitude at which the main body of data intersects the long-dashed line, and shows to what magnitude limit this sample is complete down to for that wavelength. These limits are listed in Table 2.

3 VISUAL CLASSIFICATION

3.1 Classification criteria

Perhaps the most simplistic and robust means by which a sample of galaxies may be classified into their appropriate morphological types is by visual 'eyeball' inspection. We create three-colour postage-stamp images for each galaxy in our GAMAnear sample of 3727 objects using the PI plotting tool, an internal GAMA software product.[6] For our analysis, we opt to take red, green and blue colours from the UKIDSS H and SDSS i and g bands, respectively.

[5] GAMA spectroscopic redshifts are assigned a quality from 0 to 4, where 0 is a corrupted/bad spectrum and therefore a meaningless associated redshift, and 4 is a high-quality redshift with a high degree of certainty. Typically, we advocate using $Q > 2$ for scientific analyses.

[6] A web version of this tool exists at the following web address: http://thuban4.st-and.ac.uk/gama/colcutout/gamacutout.php

Table 2. Absolute Sérsic magnitude limits, galaxy number counts and absolute solar magnitudes. Sérsic limits denote the faint-end absolute magnitude at which the sample is complete for that band. Limits are defined as the absolute magnitude at which the main body of data in the colour–magnitude diagrams of Fig. 2 intersect the volume-limited sample faint-end limit of $M_r = -17.4$. The number of galaxies refers to the how many galaxies from the GAMAnear sample are brighter than the limit in that band. The absolute magnitude of the Sun in all passbands is also shown, for reference.

Band	*u*	*g*	*r*	*i*	*z*	*Y*	*J*	*H*	*K*
Limit	−16.9	−17.3	−17.4	−17.8	−18.1	−18.2	−18.2	−18.3	−18.1
Number of galaxies below limit	2841	3445	3727	3536	3342	3195	3196	3236	3197
$M_{\odot}$	6.38	5.15	4.71	4.56	4.54	4.52	4.57	4.71	5.19

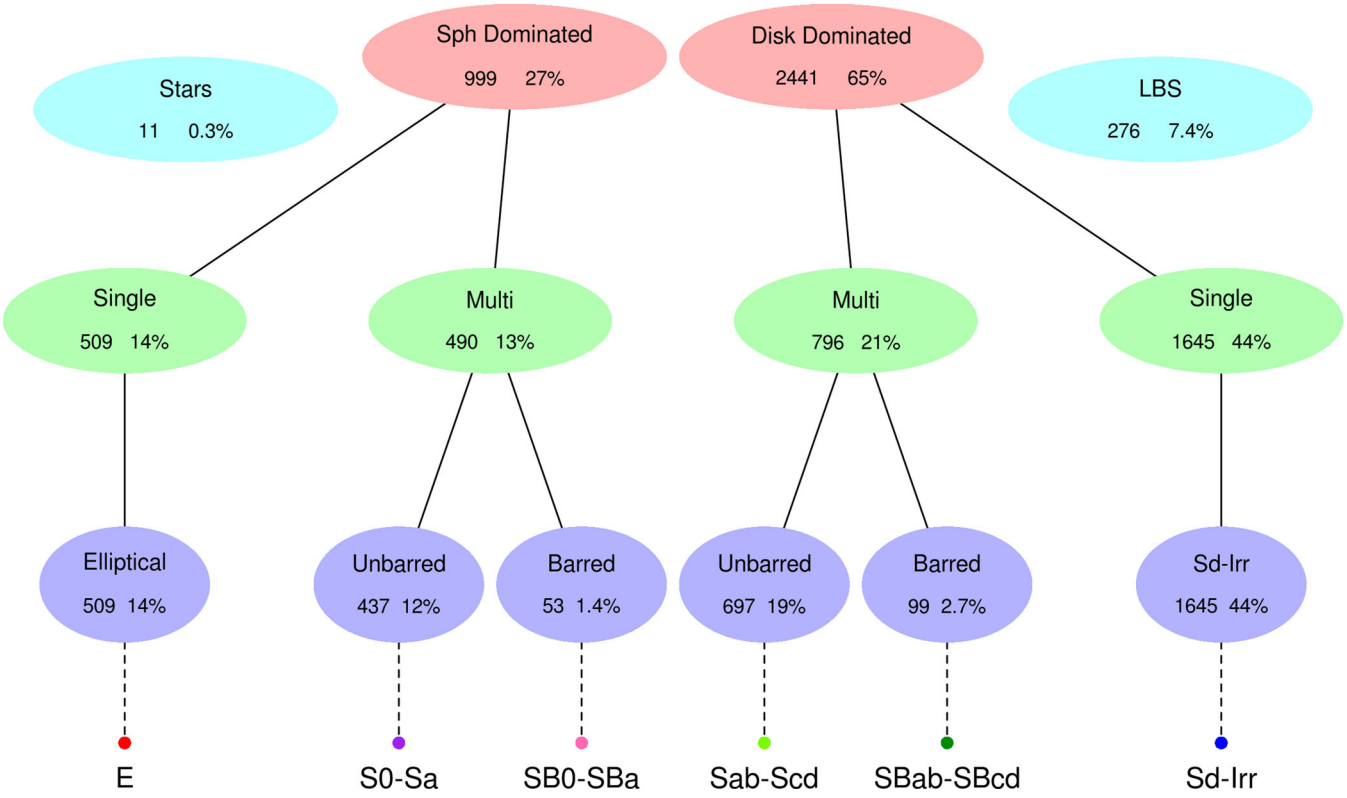

Figure 3. The morphological classification hierarchy used to filter the volume-limited GAMAnear sample of 3727 galaxies into their appropriate class. In brief: is the galaxy spheroid or disc dominated?; is the galaxy a single-component or a multicomponent system ('single' and 'multi')?; and, if the galaxy is a multicomponent system, does it contain a bar ('unbarred' and 'barred')? At the top level, the classes 'stars' and LBS are also available. See the text for further details. Beneath each label are the number of galaxies in the master classification bin for that group and an indication of the fraction of our total sample this group constitutes. The final morphological type at the bottom of this figure depends upon the prior decisions made by the classifier.

Eyeball classification occurs in two phases. Phase 1 postage stamps depict 20 arcsec × 20 arcsec with the dynamic range of the images scaled logarithmically and prior decisions made on the lower (black) and upper (white) cut levels. Phase 2 postage stamps depict a larger area of 40 arcsec × 40 arcsec and are scaled using the arctan function. We found that the arctan function removes the necessity for a harsh upper or lower cut level. Imposing harsh cuts has the potential to lead to misclassification as it imposes an apparent physical boundary in the light profile of a galaxy where none exists. The increased area of the phase 2 postage stamps also allows for the galaxy to be put into context of its local environment, and allows the observer to see more than the core of nearby extended galaxies.

Classification occurs by assigning the postage stamp of a galaxy into a specific directory hierarchy. A schematic representation of this hierarchy is shown in Fig. 3, with final 'master' number counts inset for later reference. Postage-stamp images are populated at the top level, and visual classification decisions eventually filter a galaxy down through this classification tree into its appropriate morphological class, from E to Sd-Irr, as indicated. The decision tree is essentially binary at each level (with the exception of stars and the 'little blue spheroid' classes). These levels are spheroid dominated/disc dominated, single/multi and barred/unbarred, and are discussed here.

Spheroid-dominated/disc-dominated galaxies are initially split into spheroid or disc dominated.[7] Colour may be a useful indicator here; however, the apparent gradient and smoothness of the light profile and the central concentration are the main discerning factors.

[7] Here, the terms 'spheroid dominated' and 'disc dominated' do not refer to the spheroidal or disc component dominating the total flux of the system. As has been shown in Graham & Worley (2008), rarely does the spheroid component in a bulge+disc system contribute >50 per cent of the flux for galaxies later than S0. Rather, we define the term 'spheroid dominated' and 'disc dominated' to refer to the visual impact of the spheroid or the disc on the postage-stamp images: a combination of relative size, apparent surface brightness and 2D light profile.

Single/multi: a question of the total number of distinct structural components comprising the galaxy. Spheroid-dominated single-component galaxies are classical elliptical systems, whereas spheroid-dominated multicomponent galaxies are lenticular or early-type spiral systems (S0-Sa). Disc-dominated single-component galaxies are bulge-less disc systems or irregulars (Sd-Irr), whereas disc-dominated multicomponent galaxies are late-type spiral systems (Sab-Scd).

Barred/unbarred: the final level of classification determines whether a multicomponent system contains a bar structure. If the disc is edge-on, and the presence of a bar cannot be verified, then the galaxy is classified as unbarred.

At the spheroid-dominated/disc-dominated level of classification, two additional classification options are available: stars and 'little blue spheroids' (LBS). As noted above, this is the only occasion on which the classification question is not binary.

Stars: if the primary object in the postage stamp depicts either a foreground star in front of a background galaxy (to which the associated redshift belongs) or a supernova within a distant galaxy, it is classified as a star. These objects are removed from the classification tree at the top level. This class of object is removed in all subsequent scientific analyses unless specifically mentioned in the text.

Little blue spheroids (LBS): prior to classification it became apparent that an additional type of galaxy which lies outside the standard Hubble–Jeans tuning fork exists within our sample. These galaxies are typically compact, spheroidal and blue; hence, their designation as 'little blue spheroids' (LBS from here). The median colour of our LBS sample is $g - i \sim 0.6$ with a median Sérsic index of $n_r \sim 1.9$ in the r band ($n_K \sim 1.6$ in the K band) and a median physical size of $r_e \sim 1.1$ kpc in the r band ($r_e \sim 0.9$ kpc in the K band). LBS-type galaxies may come about via the intermittent stochastic star formation predicted in low-mass dwarf galaxies by Stinson et al. (2007), and have been previously isolated observationally by Arp (1965), Sandage & Binggeli (1984) and Guzman et al. (1997), and more recently by Brough et al. (2011) and Bauer et al. (2013), amongst others. Brough et al. (2011) find that these systems are predominantly of low mass and found in low-density environments, showing similar properties to dwarf irregular galaxies in the Local Volume. For the purposes of this study, these objects are removed from the classification tree at the top level.

Three observers, LSK, SPD and ASGR, independently classified the entire sample of 3727 galaxies using both the phase 1 and phase 2 postage-stamp images. Phase 2 postage-stamp images are initially placed into their phase 1 hierarchy positions as assigned by their classifier in order to speed up and improve the second round of classification.

3.2 Classification results

A final master classification is assigned based on majority agreement. In most cases (i.e. single/multi and barred/unbarred), this requires the agreement of at least two observers. At the top level (spheroid dominated/disc dominated, stars, LBS), there is a possibility that all three observers disagree on the classification. In this instance, a preference is applied to each observer by order of classification experience (in order: SPD, ASGR, LSK). Should a disagreement arise, the classification will default to the preferred observer. These weights also apply at lower levels should a classifier have already been removed from a classification tree at the top level. At the top level, there are 56 such three-way disagreements in our combined GAMAnear sample of 3727 objects (1.5 per cent). In addition, a total of 451 objects (12.1 per cent) were classified as either 'star' or 'LBS' by at least one observer. A visual representation of the level of agreement between classifiers on the three standard questions (spheroid dominated/disc dominated, single/multi, barred/unbarred) is shown in Fig. 4.

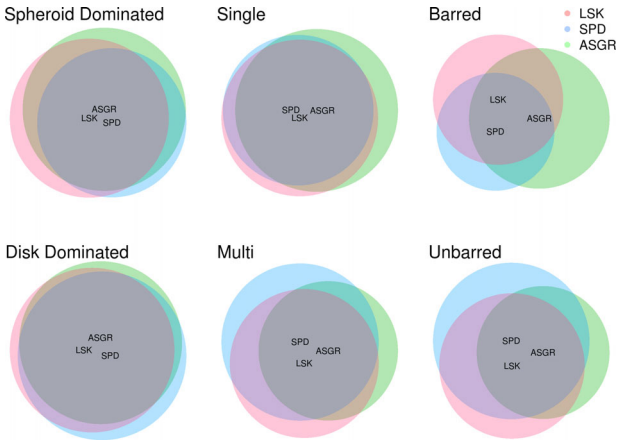

Figure 4. Euler diagrams representing the level of agreement between the three visual classifiers (LSK, SPD and ASGR) for the six main decision tree classifications: spheroid dominated/disc dominated, single/multi and barred/unbarred. Objects where any single classifier classified the system as either 'star' or 'LBS' (451 in total) have been removed from this figure, for clarity.

Generally there is good agreement between observers, however; all three observers show a noticeable disagreement on whether a system hosts a bar, which may explain the relatively low bar fraction in our galaxy sample. For our eight classification bins, we find the following three-way agreement fractions: spheroid dominated: 19.2 per cent (714); disc dominated: 56.5 per cent (2107); single: 41.9 per cent (1563); multi: 23.5 per cent (877); barred: 2.1 per cent (77); unbarred: 17.7 per cent (659); stars: 0.08 per cent (3); LBS: 2.5 per cent (95).

On combining these classification results using the method outlined above, just under half of our sample, 44.1 per cent (1, 645), is visually classified as Sd-Irr type, with elliptical galaxies accounting for 13.7 per cent (509) of the sample. Spheroid-dominated multicomponent systems account for 13.1 per cent (490) of the sample, of which 10.8 per cent (53) are visually barred. Disc-dominated multicomponent systems account for 21.4 per cent (796) of the sample, of which 12.4 per cent (99) are visually barred. Additionally, 0.3 per cent (11) of our sample are classified as 'stars' and 7.4 per cent (276) as 'LBS'. These classifications shall be used throughout the remainder of this study.

Example grey-scale postage-stamp images for the various visual morphological classes are shown in Fig. 5, arranged according to local flow-corrected redshift. The star and LBS classes are included here for reference. A comparison between our own morphological classifications and those of Galaxy Zoo can be found in Appendix B, and further three-colour postage-stamp examples for each morphological class arranged into a colour–Sérsic index plane may be found in Appendix C.

4 MORPHOLOGICAL TRENDS

4.1 Trends with global properties

In Fig. 6, we show five global galaxy measurements against one another, coloured according to their morphological classification.

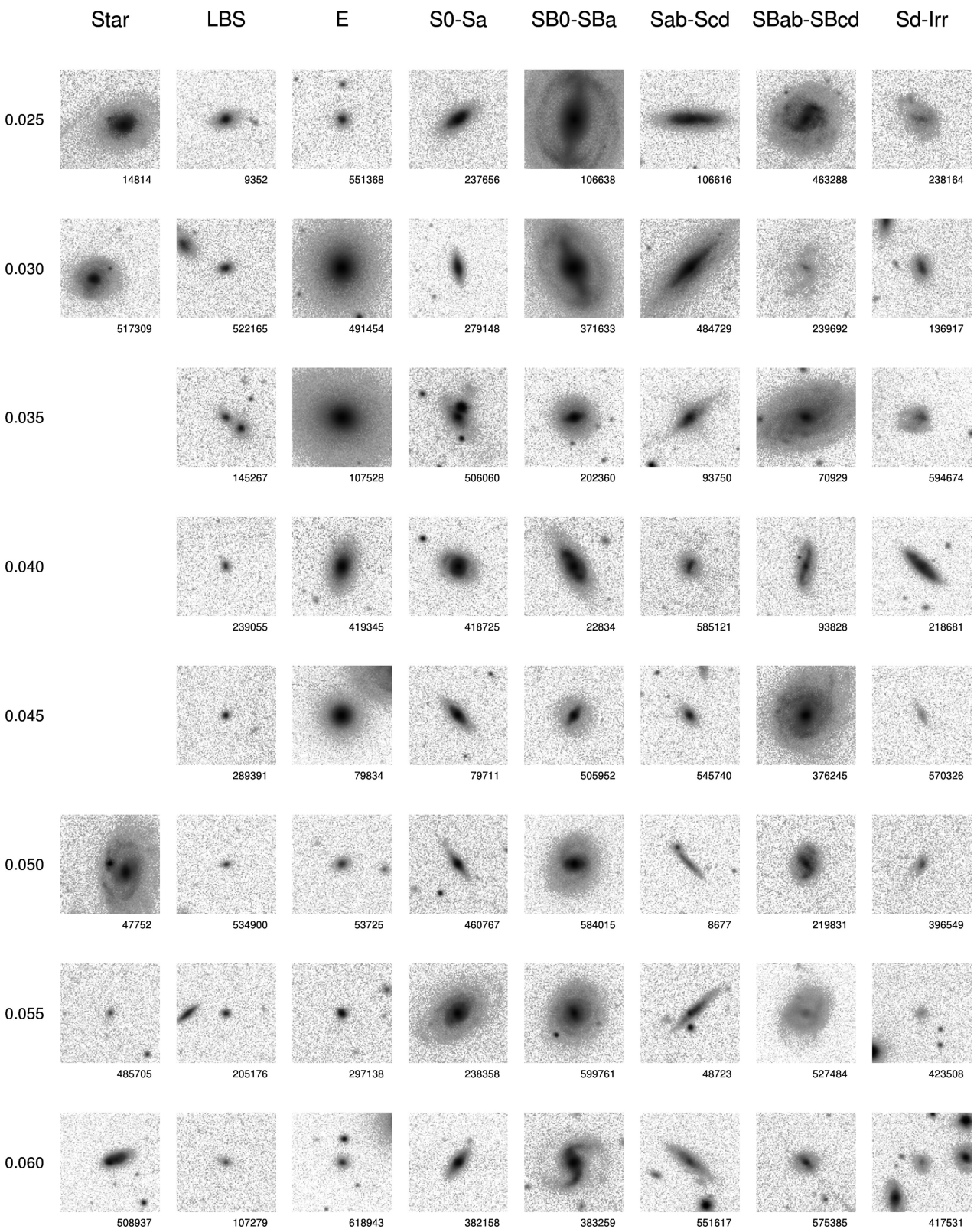

Figure 5. Example postage-stamp cutouts for each morphological class, arranged according to redshift. Below each postage stamp is the GAMA ID of the galaxy, for reference. The images shown here are created from arctan-scaled composite three-colour images (RGB taken from *Hig*, respectively), with the colours desaturated and inverted to create a grey-scale black-on-white image. Blank spaces show regions where no objects of that class exist.

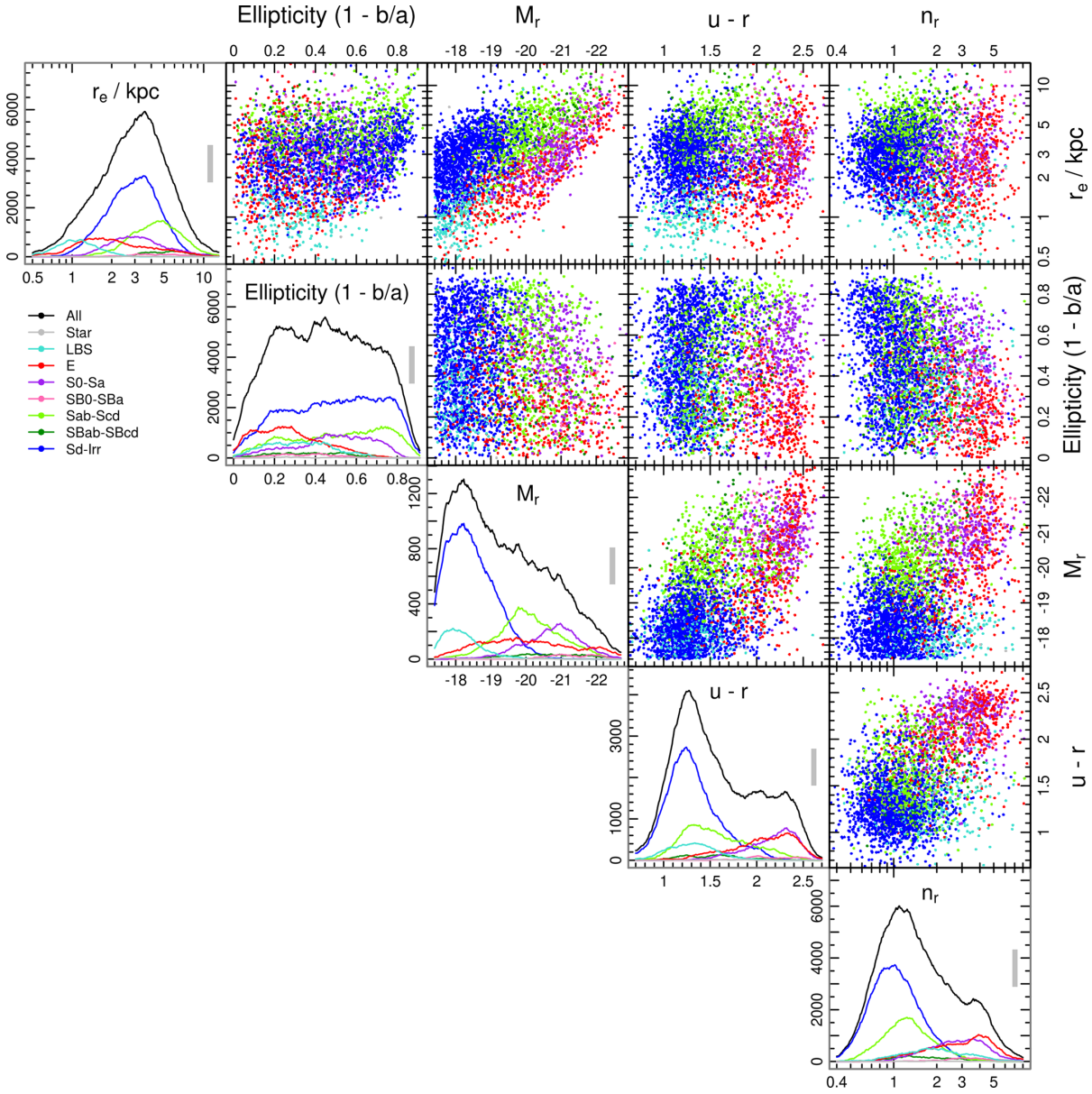

Figure 6. Correlation matrix showing five global parameters, namely (from left to right): r-band half-light radius (in kpc), ellipticity, absolute r-band Sérsic magnitude, $(u - r)$ rest-frame colour from SED fitting and r-band Sérsic index. The associated 1D density plots have been constructed using rectangular bandwidth standard deviations of 0.15, 0.09, 0.55, 0.2 and 0.13, respectively, as indicated by the width of the grey rectangles inset into each density sub-plot. The density plots integrate to the total number of objects in each population. Data points are coloured according to their visual morphological classification, as indicated. Distinct groupings of similar colour data points (i.e. same morphology) can be seen, particularly in the case of absolute magnitude against half-light radius where the red sequence for elliptical galaxies and the blue cloud for Sd-Irr-type galaxies are clearly visible.

The five measurements shown are r-band measured half-light radius (kpc), ellipticity as measured in the r band, absolute r-band Sérsic magnitude (truncated at $10r_e$), rest-frame $(u - r)$ colour from the best-fitting spectral energy distribution (SED) and r-band Sérsic index. Sérsic measurements come about from a single-Sérsic fit to the r-band data (Kelvin et al. 2012). Absolute Sérsic magnitudes are calculated in the standard sense, using equation (2).

It can be seen that some projections of the data more easily allow distinct morphological groupings to be brought out than others. Absolute magnitude against half-light radius shows a red-sequence of elliptical-type galaxies progressing from the bright extended end diagonally downwards towards the compact faint region of the figure, slightly exhibiting the curvature that is known to become more apparent at magnitudes fainter than that sampled here (e.g. Binggeli, Sandage & Tarenghi 1984; Forbes et al. 2008; Graham & Worley 2008; Misgeld & Hilker 2011). Note the elliptical galaxy extension of this curved relation in $L-r_e$ space directly into the LBS regime. Clear bimodalities in the data can be seen in the planes of absolute magnitude versus $(u - r)$ colour, absolute magnitude versus Sérsic index and $(u - r)$ colour versus Sérsic index. As has been shown in, e.g., Baldry et al. (2004), Driver et al. (2006) and Conselice (2006), these bimodal distributions are well fitted by a double-Gaussian profile.

Spheroid-dominated bulge+disc systems (S0-Sa/SB0-SBa) all occupy the same parameter space as the single-component elliptical galaxies, lying on top of the red sequence. These results are in

good agreement with the conclusions of Drory & Fisher (2007), who find that spiral galaxies harbouring classical bulges lie consistently on the red sequence. However, we do not assert that all S0-Sa galaxies harbour a classical bulge, as has previously been shown for the S0-type galaxy NGC 2787 (Erwin et al. 2003). Although speculation remains as to how $z = 0$ classical bulges came into existence, one hypothesis (Driver et al. 2013) is that they may have formed from the compact elliptical galaxies at $z \sim 2 \pm 0.5$. The evolutionary path of these high-redshift compact galaxies may have diverged from today's classical bulges, having grown a disc through gas accretion (e.g. Navarro & Benz 1991; Steinmetz & Navarro 2002; Graham 2013) while today's elliptical galaxies puffed-up via progressive minor accretion events (see Driver et al. 2013, and references therein), but see Carollo et al. (2013). In contrast to classical bulges, pseudo-bulges are believed to form via secular evolutionary processes present within the disc (Debattista et al. 2006; Gadotti 2009; Saha, Martinez-Valpuesta & Gerhard 2012). In brief: if left in isolation for a sufficient length of time (i.e. without any major merging events), a dynamically cold rotating disc system will form a barred structure. In practice, external gravitational triggers (flybys, rather than mergers) are additionally responsible for inducing the formation of bars. The bar acts as a very efficient means by which stellar mass and gas in the disc may be funnelled into the core of the galaxy, initiating a new phase of star formation in the central region. A young, blue sub-structure exhibiting a large component of angular velocity and a flattened 2D-like structure with a low central concentration (Sérsic $n \lesssim 2$) will form. This new structure is commonly referred to as a pseudo-bulge. We note however that it is possible to form low Sérsic index ($n < 2$) bulges via other non-secular processes (see a full review in Graham 2013). Unlike classical bulges, Drory & Fisher find that galaxies with pseudo-bulges typically lie in the blue cloud (Drory & Fisher 2007). We find very few multicomponent systems overlapping with the main body of the blue cloud, and conclude that structural decomposition is required in order to comment further on (a) which of these galaxies may contain a pseudo-bulge and (b) where these galaxies lie in relation to the blue cloud.

4.2 Trends with redshift

One would not expect to see large evolutionary variations in morphological fraction over a narrow redshift range such as that used in the creation of our volume-limited sample. Fig. 7 shows the data as a function of redshift, with data points coloured according to their morphology, as indicated. These data are shown relative to their absolute r-band Sérsic magnitudes (top) and number fractions (bottom). Shaded regions indicate $\pm 1\sigma$ binomial confidence intervals (Cameron 2011). One can clearly see the large-scale structure with redshift appearing as overdense strips in the scatter plot. The two distinctive peaks in the Sd-Irr-type galaxy population at redshifts of low density ($z \sim 0.035$ and $z \sim 0.047$) reflect the aforementioned morphology–density relation of Dressler (1980).

Elliptical galaxies (red) exhibit a minor fractional evolution over this redshift range, with a higher proportion of elliptical galaxies at the high redshift end of our sample relative to our lowest redshift bin. Moving from high to low redshift, as the elliptical fraction drops off it is replaced by Sab-Scd (and, to a lesser extent, SBab-SBcd) type galaxies. However, these trends appear to be minor, and confirm that these data do not show large evolutionary variations in morphological fraction with redshift. Note that we did observe distinct fractional evolutionary trends at redshifts below $z = 0.025$, i.e. our lower limit; however, we give low credence to these results

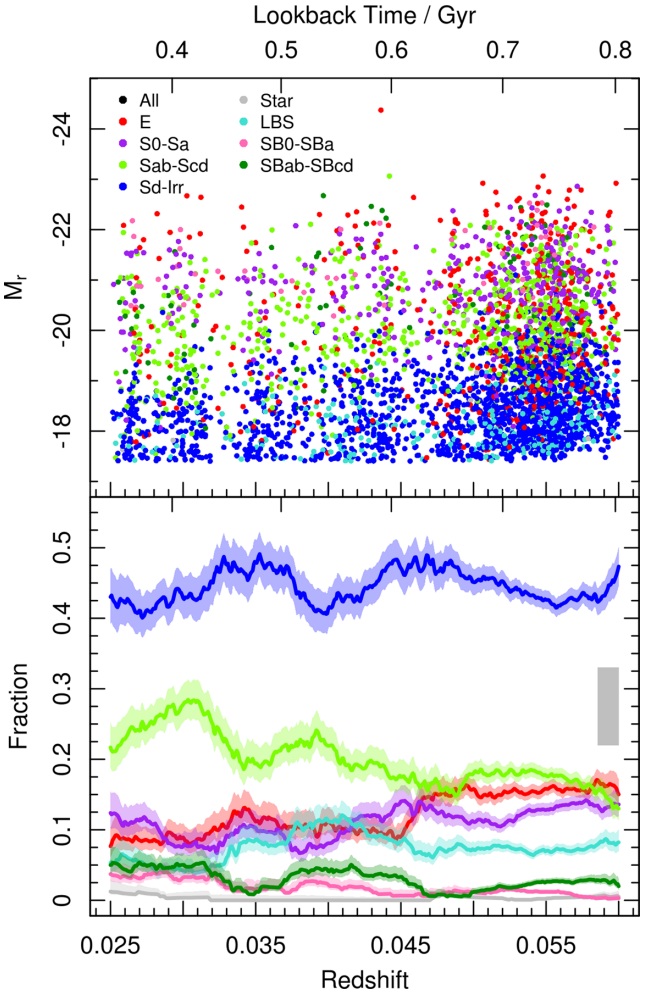

Figure 7. Morphology against redshift. Data points are coloured according to their morphology, as indicated. (top) Absolute r-band Sérsic magnitude as a function of redshift. (bottom) The representative fractions of the total number of galaxies for each morphology, as a function of redshift. Shaded regions indicate $\pm 1\sigma$ binomial confidence intervals (Cameron 2011). These fractions have been constructed using a rectangular kernel with a bandwidth standard deviation of 0.005, as indicated by the width of the grey rectangle inset into the lower plot.

owing to the very low numbers of galaxies in our volume at $z < 0.025$ ($\sim$300 galaxies in the redshift range $0.013 < z < 0.025$).

5 LUMINOSITY FUNCTIONS

The luminosity function (LF) describes the number density of galaxies in any given luminosity (or magnitude) bin across a wide range of luminosities. Measurement of the LF allows for constraints to be placed on galaxy formation and evolution models, and as such is valuable and informative.

5.1 The Schechter LF

The Schechter (1976) LF is an analytical representation of the LF, describing the number of galaxies per unit volume in the luminosity interval L to $L + \mathrm{d}L$, where $\mathrm{d}L$ is some linear luminosity interval. The number density, $\phi(L)\mathrm{d}L = \mathrm{d}n$, is given by

$$\phi(L)\,\mathrm{d}L = \phi^* \left(\frac{L}{L^*}\right)^{\alpha} \exp\left(-\frac{L}{L^*}\right) \frac{1}{L^*}\mathrm{d}L, \qquad (3)$$

where ϕ^* is the normalization constant, L^* is the characteristic luminosity describing the position of the 'knee' in the LF and α gives the slope of the LF at the faint end (where $L \ll L^*$). Note that ϕ^*, L^* and α are to be determined by minimizing a fit to the data. The impact of the Schechter function is to truncate the bright-end power-law distribution of galaxies, vastly reducing number counts at luminosities brighter than L^*.

It is usually more convenient when considering luminosities to re-write the Schechter function in terms of magnitude, as given by

$$\Phi(M)\,\mathrm{d}M = 0.4 \ln 10 \cdot \phi^* 10^{-0.4(M-M^*)(\alpha+1)} \times \exp\left(-10^{-0.4(M-M^*)}\right) \mathrm{d}M, \quad (4)$$

where M and M^* are the magnitude and the characteristic magnitude corresponding to L^*. The parameters α and ϕ^* now correspond to the slope and normalization constant in magnitude space. Equation (4) is the form of the Schechter function we shall assume throughout the remainder of this paper.

5.2 Measuring the LF

The total galaxy luminosity function (GLF) is dominated by large numbers of very faint galaxies, while the space density of brighter galaxies drops off sharply beyond some given luminosity (L^*). Despite their numerical dominance however, low-luminosity systems tend to contribute a relatively small fraction to the total luminosity budget of any given volume (Driver 1999). The GLF is a combination of its constituent MLFs, with each morphological type contributing variable number densities, dependent upon magnitude.

Fig. 8 shows the GLF and constituent MLFs across nine GAMA wavelengths (*ugrizYJHK*) for our volume-limited GAMAnear sample of 3727 galaxies. The barred populations have been merged into their sibling classes owing to low number statistics for those two populations. Each population (total and morphological type) is binned into absolute Sérsic magnitude bins of 0.25 mag and fitted with a single-Schechter function.[8] Errors on each bin are assumed to be Poissonian. Shaded grey areas indicate the limits of the fit beyond which data were not used to constrain the Schechter function model. These limits are a minimum number count of $n \leq 3$ and an absolute Sérsic magnitude faint-end cutoff as given in Table 2.

The knee in the total Schechter function progresses smoothly towards brighter AB magnitudes as one moves from u to K, as expected. We find the knee to be generally well fitted with a single-Schechter function until $\sim z$ band. At longer wavelengths, the GLF appears to require a secondary component to aid in fully reproducing the downturn at the bright end and the secondary upturn at the faint end.

These data provide one of the first measurements of the MLF using Sérsic photometry, and provide a key insight into the nature of the underlying galaxy populations. Considering the morphology sub-populations alone, the faint end appears to be heavily dominated by Sd-Irr-type galaxies, in addition to a significant LBS fraction. Intermediate magnitudes typically contain both the S0-Sa- and Sab-Scd-type systems. Elliptical galaxies dominate at the brightest magnitudes; however, below their L^* knee, the number of E-type galaxies remains relatively constant across all wavelengths. The Sd-Irr and LBS populations appear to show the largest variation in their MLFs with respect to wavelength, with the faint-end slopes varying strongly from u to K as the relative depth of the data in those bands becomes shallower. Owing to our sample selection constraints and the relatively high quality of the r-band data, one would expect the M^* and α parameters for Sd-Irr- and LBS-type galaxies in the r band to be the most robust in relation to other passbands, which is perhaps evidenced by the suggestion of a downturn in the Sd-Irr-type galaxy population at the faintest ($M_r > -18.5$ mag) magnitudes. In contrast, the E, S0-Sa and Sab-Scd populations reproduce consistent LF curves at each wavelength, albeit offset in magnitude.

Single-Schechter fit parameters are shown for all populations in Tables 3 (All), 4 (LBS), 5 (E), 6 (S0-Sa), 7 (Sab-Scd) and 8 (Sd-Irr). In addition to the Schechter fit parameters, we also calculate the luminosity density for each population at each wavelength. The luminosity density, j, is the integral under the Schechter function curve and is given by

$$j = \int_0^\infty L\phi(L)\,\mathrm{d}L = \phi^* L^* \Gamma(\alpha + 2) \quad (5)$$

as in Liske et al. (2003). Note that the luminosity densities are those calculated from an extrapolation across all luminosities. Also note that the quoted errors on j are likely to be a lower bound owing to the correlation of errors in L^*, α and ϕ^*.

Alongside the characteristic knee in the Schechter LF, L^* (or M^*), the remaining fitted parameters are the slope of the faint end of the LF, α, and the normalization ϕ^*. While the error on the latter may be estimated via some simplistic method such as jackknife resampling[9] of the data set, the well-known covariance between α and M^* would result in their jackknife errors being systematically underestimated. An alternative approach is to produce error ellipses which map out the χ^2 parameter space around the best-fitting values. This technique involves re-fitting the data set fitting for ϕ^* alone while adopting a fixed pair of input α and M^* parameters as defined by a regularly spaced grid about the best-fitting values. Assuming Gaussian errors, the resultant χ^2 surface then allows for 1σ, 2σ and 3σ errors to be determined as the contours which lie at $\Delta\chi^2 = 2.30$, 6.17 and 11.8, respectively.

We thus derive error ellipses for all nine photometric bands of our data set, and show the results in Fig. 9. Error ellipses for the total GLF and the constituent MLFs are shown, as indicated. Successive contours represent the 1σ, 2σ and 3σ errors on each parameter. As can be seen, the strong covariance between these two parameters has a strong impact on each error ellipse. The LBS population shows the largest errors, which should not be surprising considering our sample selection limits and the typically faint magnitude of these systems. The visible truncation of the LBS error ellipses towards the bright end of each figure (with the exception of the r band) is as expected, owing to a lack of LBS-type systems at brighter magnitudes. The brightest LBS in our sample has a Sérsic r-band magnitude of $M_r = -20.82$ mag. Only the r-band data allow any meaningful constraints to be placed on Schechter fit parameters to the LBS population (and to some extent, the Sd population also), particularly in constraining M^*.

[8] Schechter functions are fitted to the available data within our magnitude ranges using the NLMINB routine in R; a quasi-Newton algorithm based on the PORT routines that optimize fitting in a similar sense to the Limited-memory Broyden–Fletcher–Goldfarb–Shanno (LM-BFGS) algorithm, with an extension to handle simple box constraints on input variables (L-BFGS-B). The PORT documentation is available at http://netlib.bell-labs.com/cm/cs/cstr/153.pdf.

[9] A statistical resampling method designed to estimate sample bias and variance by systematically recomputing our Schechter fit parameters on numerous sub-sets of our data.

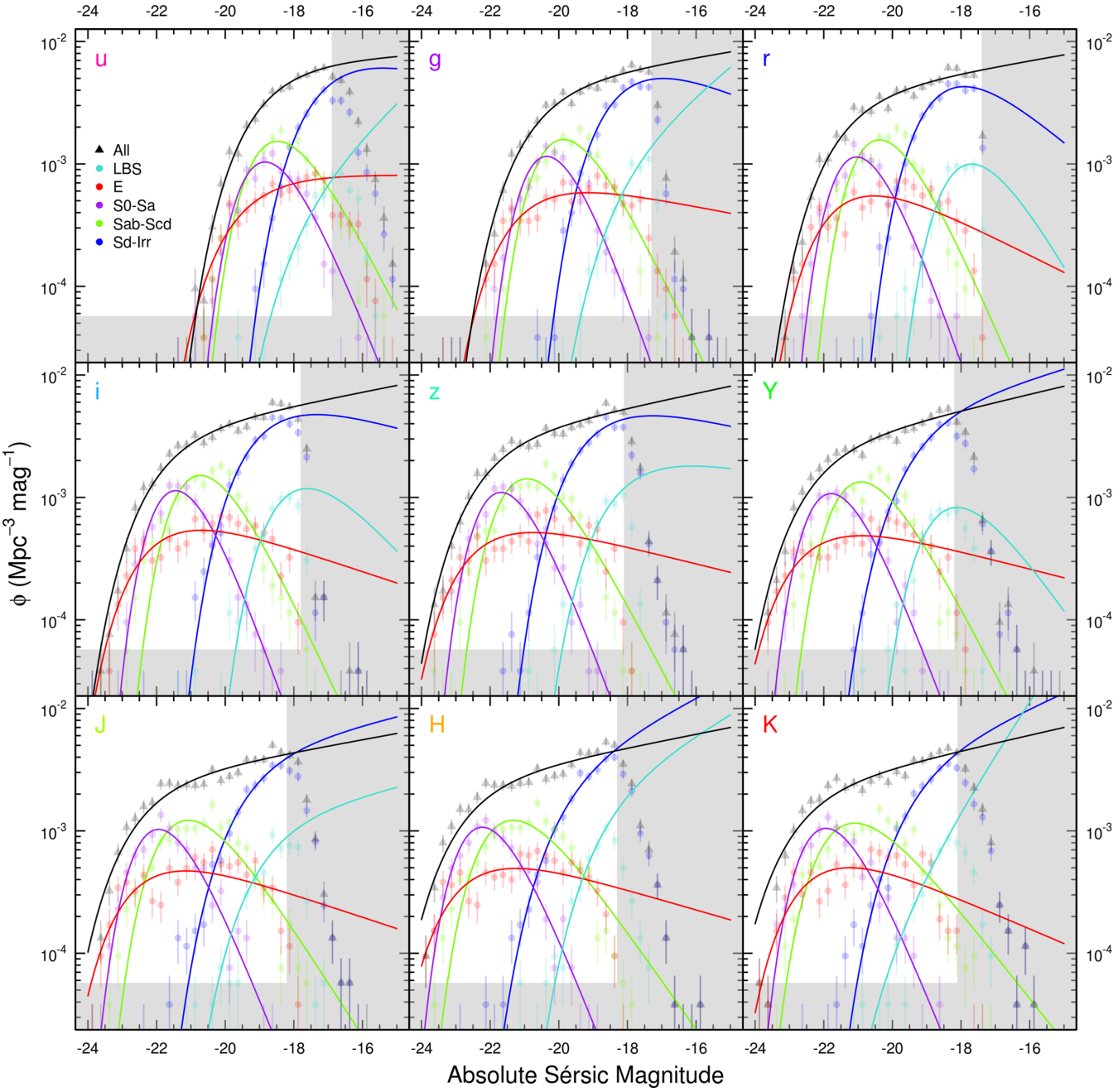

Figure 8. MLFs across all nine bands for the various morphological types (coloured points and lines, as indicated) and total populations (black points and lines). Each population has been fitted with a single-Schechter function. Prior to fitting, the data are split into bins of 0.25 mag, with the error on the measurement per bin taken as Poissonian ($\sqrt{n}$) in nature. Shaded grey areas indicate those regions where data have not been used in the fits. Variable faint-end magnitude limits are given in Table 2.

Of the standard Hubble types, the faint-end slope of the Sd-Irr class in the u band, $\alpha_u = -0.82^{+0.61}_{-0.55}$, is particularly poorly constrained owing to the poor quality and relatively shallow depth of the u band in conjunction with the completeness issues for the Sd-Irr population. Conversely, while α is typically well constrained for the elliptical populations, the value of the knee in the Schechter function is not. In the K band for example, the turnover is found at $M^*_K = -22.55^{+0.34}_{-0.38}$ mag, a relatively large uncertainty. Also note the relative consistency between recovered α values for all populations over all wavelengths, excepting the u band and LBS populations as discussed above.

The majority of the morphology sub-populations appear to be well fitted by a single-Schechter function, with reduced χ^2 values typically lying within the range $0.5 < \chi^2/\nu < 2$. The only notable exceptions to this are for the LBS and the Sab-Scd populations. The knee of the LBS population at most wavelengths lies outside the fitting limits, beyond the faint-end limit, and so the overall fit may instead be better suited by a single-exponential function. Note in Table 4 that the slope of the LBS population in the K band is so poorly constrained that the estimated luminosity density diverges; hence, no estimate of luminosity density is calculated. The faint-end limit may also affect the Sd-Irr population, particularly in the

Table 3. Single-Schechter LF fit parameters for the total GLF as shown in Fig. 8. From left to right, columns are GAMA passband; the knee in the Schechter function (M^*); the slope of the faint end of the Schechter function (α); the normalization constant of the Schechter function (ϕ^*); the χ^2 goodness of fit parameter (χ^2/ν); and the luminosity density (j). Errors on M^* and α are taken from the 1σ error ellipses shown in Fig. 9. All other errors are estimated using the relation $\sigma^2 = \frac{N-1}{N}\sum_{i=1}^{N}\left(x_j - x\right)^2$, where x is the best-fitting parameter, x_j is the best-fitting parameter as given from a jackknife resampled variant of the data set and N is the number of jackknife volumes. We adopt $N = 10$.

Band	M^* (mag)	α	$\phi^*/10^{-3}$ ($\mathrm{mag}^{-1}\,\mathrm{Mpc}^{-3}$)	χ^2/ν	$j/10^7$ ($\mathrm{L}_\odot\,\mathrm{Mpc}^{-3}$)
u	$-19.18^{+0.13}_{-0.13}$	$-1.05^{+0.09}_{-0.08}$	6.99 ± 1.60	1.12	$12.05^{+0.86}_{-0.86}$
g	$-20.95^{+0.12}_{-0.12}$	$-1.12^{+0.05}_{-0.04}$	4.71 ± 0.37	1.92	$14.00^{+0.51}_{-0.51}$
r	$-21.71^{+0.11}_{-0.11}$	$-1.12^{+0.03}_{-0.03}$	4.00 ± 0.21	2.79	$16.02^{+0.81}_{-0.81}$
i	$-22.15^{+0.10}_{-0.12}$	$-1.14^{+0.04}_{-0.03}$	3.61 ± 0.52	2.46	$19.29^{+1.39}_{-1.39}$
z	$-22.49^{+0.12}_{-0.13}$	$-1.15^{+0.04}_{-0.03}$	3.17 ± 0.22	2.32	$22.89^{+1.30}_{-1.30}$
Y	$-22.61^{+0.13}_{-0.13}$	$-1.16^{+0.03}_{-0.04}$	2.77 ± 0.37	2.25	$22.16^{+1.16}_{-1.16}$
J	$-22.78^{+0.13}_{-0.14}$	$-1.13^{+0.04}_{-0.03}$	2.72 ± 0.27	3.18	$25.90^{+1.64}_{-1.64}$
H	$-23.02^{+0.13}_{-0.13}$	$-1.14^{+0.04}_{-0.03}$	2.73 ± 0.63	4.32	$37.08^{+7.94}_{-7.94}$
K	$-23.06^{+0.19}_{-0.21}$	$-1.16^{+0.04}_{-0.04}$	2.33 ± 0.39	3.11	$52.07^{+5.63}_{-5.63}$

Table 4. As Table 3 but for LBS.

Band	M^* (mag)	α	$\phi^*/10^{-3}$ ($\mathrm{mag}^{-1}\,\mathrm{Mpc}^{-3}$)	χ^2/ν	$j/10^7$ ($\mathrm{L}_\odot\,\mathrm{Mpc}^{-3}$)
u	$-17.99^{+1.71}_{-4.22}$	$-1.65^{+2.76}_{-1.01}$	0.60 ± 1.98	0.47	$0.85^{+4.60}_{-0.85}$
g	$-18.35^{+1.15}_{-3.70}$	$-1.55^{+1.65}_{-1.07}$	1.29 ± 2.03	0.93	$0.63^{+2.27}_{-0.63}$
r	$-17.45^{+0.49}_{-0.61}$	$0.25^{+1.28}_{-1.05}$	2.87 ± 1.21	1.10	$0.24^{+0.03}_{-0.03}$
i	$-17.88^{+0.69}_{-1.21}$	$-0.21^{+1.87}_{-1.58}$	3.40 ± 2.20	1.32	$0.30^{+0.12}_{-0.12}$
z	$-18.39^{+0.97}_{-3.84}$	$-0.88^{+2.31}_{-1.75}$	2.85 ± 2.97	1.10	$0.40^{+0.93}_{-0.40}$
Y	$-18.11^{+0.75}_{-1.96}$	$0.01^{+1.65}_{-1.87}$	2.45 ± 2.62	1.47	$0.28^{+0.12}_{-0.12}$
J	$-19.06^{+1.07}_{-3.41}$	$-1.17^{+1.47}_{-1.08}$	1.33 ± 2.13	1.72	$0.43^{+1.15}_{-0.43}$
H	$-18.85^{+0.98}_{-3.29}$	$-1.40^{+2.01}_{-1.26}$	2.38 ± 3.90	0.71	$0.94^{+12.61}_{-0.94}$
K	$-20.08^{+1.94}_{-3.14}$	$-2.07^{+1.73}_{-0.59}$	0.22 ± 1.31	0.21	–

Table 5. As Table 3 but for elliptical galaxies.

Band	M^* (mag)	α	$\phi^*/10^{-3}$ ($\mathrm{mag}^{-1}\,\mathrm{Mpc}^{-3}$)	χ^2/ν	$j/10^7$ ($\mathrm{L}_\odot\,\mathrm{Mpc}^{-3}$)
u	$-19.81^{+0.46}_{-0.69}$	$-0.99^{+0.23}_{-0.22}$	0.92 ± 0.41	0.67	$2.73^{+1.10}_{-1.10}$
g	$-21.32^{+0.33}_{-0.39}$	$-0.86^{+0.11}_{-0.12}$	0.95 ± 0.21	0.96	$3.44^{+0.29}_{-0.29}$
r	$-21.67^{+0.29}_{-0.29}$	$-0.65^{+0.10}_{-0.08}$	1.22 ± 0.19	2.41	$3.88^{+0.37}_{-0.37}$
i	$-22.28^{+0.32}_{-0.36}$	$-0.77^{+0.10}_{-0.09}$	1.04 ± 0.15	1.58	$5.13^{+0.70}_{-0.70}$
z	$-22.65^{+0.29}_{-0.31}$	$-0.83^{+0.09}_{-0.08}$	0.91 ± 0.14	1.60	$6.29^{+0.43}_{-0.43}$
Y	$-22.77^{+0.31}_{-0.35}$	$-0.82^{+0.09}_{-0.08}$	0.86 ± 0.17	1.17	$6.53^{+0.50}_{-0.50}$
J	$-22.73^{+0.30}_{-0.34}$	$-0.77^{+0.09}_{-0.08}$	0.91 ± 0.22	2.27	$6.89^{+0.75}_{-0.75}$
H	$-22.98^{+0.31}_{-0.33}$	$-0.80^{+0.09}_{-0.08}$	0.91 ± 0.15	1.91	$9.91^{+0.98}_{-0.98}$
K	$-22.55^{+0.34}_{-0.38}$	$-0.70^{+0.10}_{-0.09}$	1.05 ± 0.21	3.07	$11.76^{+1.96}_{-1.96}$

estimation of the faint-end slope, as can be seen in Fig. 9. The Sab-Scd population is well described by a single-Schechter fit for systems fainter than $M_r \sim -21$ mag, however; at brighter magnitudes the Sab-Scd population departs from a single-Schechter form, with number counts at brighter magnitudes very closely matching

Table 6. As Table 3 but for S(B)0-S(B)a galaxies.

Band	M^* (mag)	α	$\phi^*/10^{-3}$ ($\mathrm{mag}^{-1}\,\mathrm{Mpc}^{-3}$)	χ^2/ν	$j/10^7$ ($\mathrm{L}_\odot\,\mathrm{Mpc}^{-3}$)
u	$-18.20^{+0.18}_{-0.18}$	$0.80^{+0.31}_{-0.26}$	2.37 ± 0.24	1.53	$2.71^{+0.22}_{-0.22}$
g	$-19.55^{+0.17}_{-0.17}$	$1.09^{+0.31}_{-0.26}$	2.17 ± 0.19	1.45	$3.61^{+0.28}_{-0.28}$
r	$-20.25^{+0.17}_{-0.16}$	$1.08^{+0.30}_{-0.25}$	2.16 ± 0.29	1.60	$4.50^{+0.34}_{-0.34}$
i	$-20.67^{+0.16}_{-0.16}$	$1.04^{+0.29}_{-0.24}$	2.22 ± 0.25	1.18	$5.72^{+0.49}_{-0.49}$
z	$-20.97^{+0.17}_{-0.17}$	$0.94^{+0.28}_{-0.25}$	2.31 ± 0.18	1.23	$6.99^{+0.51}_{-0.51}$
Y	$-21.08^{+0.15}_{-0.15}$	$0.93^{+0.26}_{-0.23}$	2.27 ± 0.32	0.71	$7.39^{+0.62}_{-0.62}$
J	$-21.30^{+0.16}_{-0.16}$	$0.82^{+0.25}_{-0.22}$	2.33 ± 0.37	1.25	$8.82^{+0.80}_{-0.80}$
H	$-21.58^{+0.15}_{-0.16}$	$0.82^{+0.24}_{-0.21}$	2.43 ± 0.32	0.87	$13.63^{+1.36}_{-1.36}$
K	$-21.31^{+0.16}_{-0.17}$	$0.78^{+0.26}_{-0.22}$	2.43 ± 0.17	1.03	$16.02^{+1.19}_{-1.19}$

Table 7. As Table 3 but for S(B)ab-S(B)cd galaxies.

Band	M^* (mag)	α	$\phi^*/10^{-3}$ ($\mathrm{mag}^{-1}\,\mathrm{Mpc}^{-3}$)	χ^2/ν	$j/10^7$ ($\mathrm{L}_\odot\,\mathrm{Mpc}^{-3}$)
u	$-18.10^{+0.21}_{-0.22}$	$0.41^{+0.31}_{-0.28}$	4.20 ± 0.27	2.03	$3.27^{+0.28}_{-0.28}$
g	$-19.43^{+0.17}_{-0.15}$	$0.51^{+0.19}_{-0.17}$	4.19 ± 0.16	3.20	$3.80^{+0.37}_{-0.37}$
r	$-19.83^{+0.19}_{-0.19}$	$0.65^{+0.22}_{-0.19}$	3.90 ± 0.30	4.54	$3.81^{+0.47}_{-0.47}$
i	$-20.25^{+0.18}_{-0.19}$	$0.54^{+0.20}_{-0.18}$	3.95 ± 0.16	4.33	$4.55^{+0.48}_{-0.48}$
z	$-20.60^{+0.18}_{-0.17}$	$0.36^{+0.17}_{-0.15}$	3.96 ± 0.10	3.79	$5.44^{+0.54}_{-0.54}$
Y	$-20.57^{+0.18}_{-0.18}$	$0.37^{+0.17}_{-0.15}$	3.72 ± 0.13	4.73	$4.95^{+0.49}_{-0.49}$
J	$-20.97^{+0.17}_{-0.17}$	$0.10^{+0.14}_{-0.11}$	3.59 ± 0.41	3.46	$6.19^{+0.74}_{-0.74}$
H	$-21.32^{+0.18}_{-0.18}$	$0.01^{+0.13}_{-0.12}$	3.61 ± 0.23	3.57	$9.38^{+1.02}_{-1.02}$
K	$-21.23^{+0.17}_{-0.16}$	$-0.11^{+0.12}_{-0.10}$	3.40 ± 0.29	3.35	$12.03^{+1.04}_{-1.04}$

Table 8. As Table 3 but for Sd-Irr galaxies.

Band	M^* (mag)	α	$\phi^*/10^{-3}$ ($\mathrm{mag}^{-1}\,\mathrm{Mpc}^{-3}$)	χ^2/ν	$j/10^7$ ($\mathrm{L}_\odot\,\mathrm{Mpc}^{-3}$)
u	$-17.26^{+0.33}_{-0.39}$	$-0.82^{+0.61}_{-0.55}$	10.74 ± 2.81	0.42	$2.84^{+0.74}_{-0.74}$
g	$-18.25^{+0.23}_{-0.27}$	$-0.70^{+0.32}_{-0.29}$	10.55 ± 1.17	1.72	$2.17^{+0.12}_{-0.12}$
r	$-18.46^{+0.16}_{-0.16}$	$-0.40^{+0.22}_{-0.19}$	11.56 ± 0.50	1.08	$1.91^{+0.06}_{-0.06}$
i	$-19.07^{+0.23}_{-0.24}$	$-0.80^{+0.26}_{-0.23}$	8.73 ± 1.33	2.09	$2.27^{+0.13}_{-0.13}$
z	$-19.24^{+0.24}_{-0.26}$	$-0.84^{+0.29}_{-0.26}$	7.97 ± 1.38	1.55	$2.40^{+0.15}_{-0.15}$
Y	$-19.52^{+0.29}_{-0.34}$	$-1.20^{+0.27}_{-0.26}$	5.26 ± 1.86	0.73	$2.54^{+0.30}_{-0.30}$
J	$-19.54^{+0.34}_{-0.39}$	$-1.17^{+0.32}_{-0.29}$	4.65 ± 0.98	1.66	$2.31^{+0.13}_{-0.13}$
H	$-19.97^{+0.36}_{-0.44}$	$-1.36^{+0.31}_{-0.27}$	3.66 ± 1.50	1.47	$3.82^{+0.60}_{-0.60}$
K	$-19.59^{+0.45}_{-0.54}$	$-1.31^{+0.41}_{-0.34}$	3.97 ± 1.70	2.52	$4.25^{+0.82}_{-0.82}$

those of the S0-Sa population. We find that a double-Schechter fit to this Sab-Scd population is similarly recalcitrant, and so we elect to maintain a single-Schechter fit to the Sab-Scd population.

It is evident however that at wavelengths longer than the z band, a single-Schechter fit to the total GLF is a poor fit, reaching a peak goodness of fit value of $\chi^2/\nu = 4.31$ in the H band. This is as expected if one considers that the field galaxy LF is comprised of an initial red spheroidal 'bump' at bright magnitudes and then a subsequent blue disc 'bump' at fainter magnitudes, as can clearly be seen in Fig. 8 and noted in, e.g., Phillipps & Driver (1995), Popesso et al. (2006) and Loveday et al. (2012). A single-Schechter function is unable to account for the intricacy in this distribution.

We elect to fit the total GLF with a double-Schechter function with a shared knee, while maintaining single-Schechter fits to the

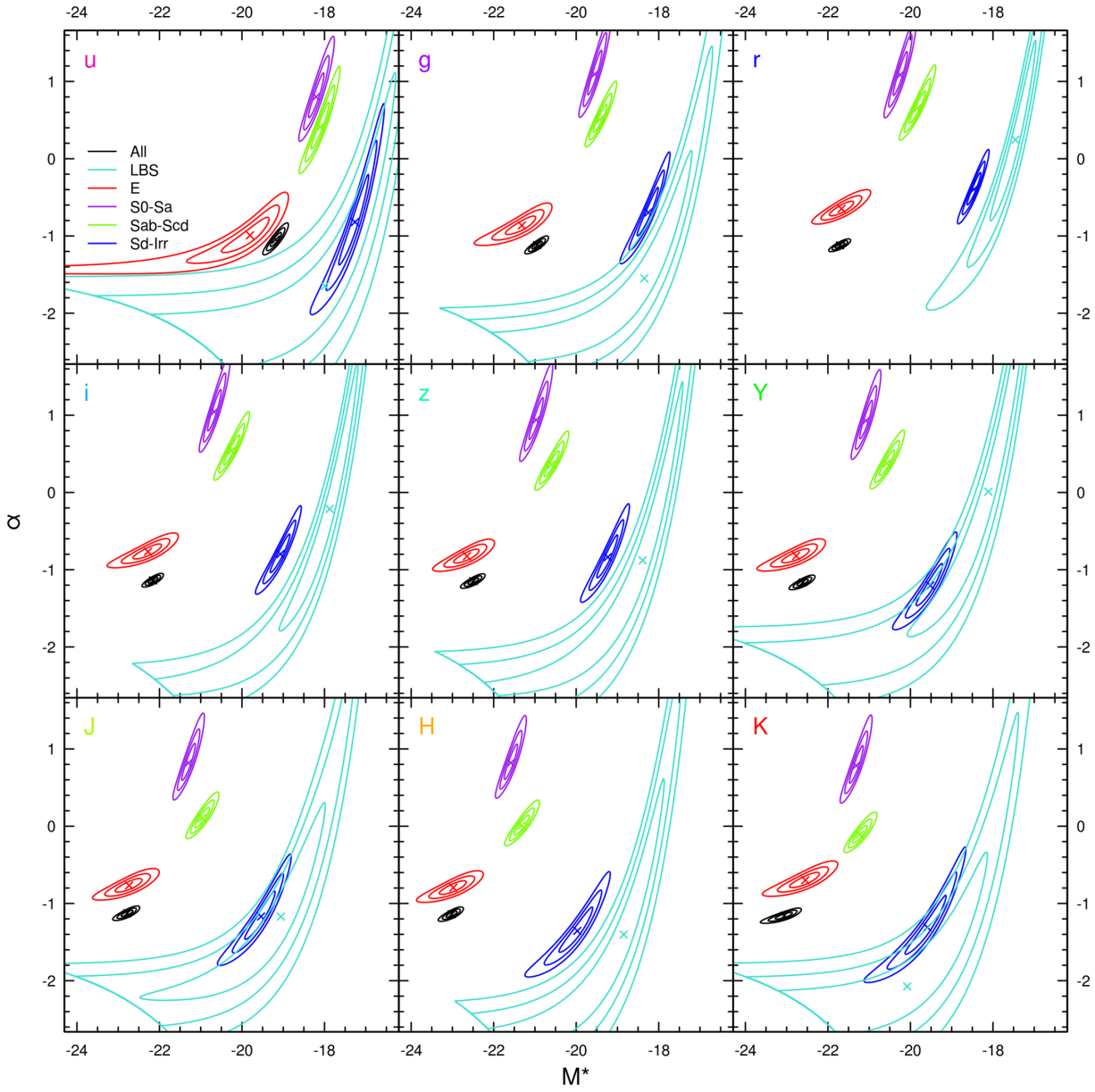

Figure 9. Error ellipses for each Schechter function fit shown in Fig. 8. These ellipses are generated by constructing a regularly spaced grid of input M^* and α values in steps of 0.01 each and fitting for the normalization constant ϕ^* in the Schechter function, producing a χ^2 map about the coordinates of the best fit. Successive contours represent the 1σ, 2σ and 3σ error boundaries ($\Delta\chi^2 = 2.30$, 6.17 and 11.8, respectively). Note the significant diagonal elongation between these parameters, particularly for the Sd class population. This highlights the covariant relationship between M^* and α.

morphology sub-populations. The free parameters for the double-Schechter fit are M^*, α_1, ϕ_1^*, α_2 and ϕ_2^*. The results of this fit are shown in Fig. 10 for all nine bands, and the fit parameters given in Table 9. It is instantly apparent once more that the GLF is more naturally fitted with a double-Schechter function than a single-Schechter function, particularly so for the longer NIR wavelengths. All χ^2 values beyond the z band show a significant improvement in the quality of the fit. However, the shortest wavelengths show little need for the extra parameters, with the goodness of fit showing a mild worsening in the u band, again most likely owing to the poorer quality of the u-band data. Nevertheless, the overall fits appear robust, and so we advocate a double-Schechter form for the field total GLF but a single-Schechter function forms for the morphology sub-population MLFs.

A summary of both the single- and double-Schechter fits to the GLF in addition to the adopted single-Schechter fits to the MLFs in the r band is shown in Fig. 11. Also shown are several other contemporary single-Schechter fits to similar r-band data, scaled to our preferred cosmology of $(H_0, \Omega_m, \Omega_\Lambda) = (70, 0.3, 0.7)$ and k-corrected where necessary from $r^{0.1}$ back to a $z = 0$ rest frame using a typical correction of $k_{0.1} = 0.12$. There is generally good agreement between our global LF fits and those of other studies. The variable faint-end limit between surveys makes a comparison of the faint-end slope problematic; however, the M^* and ϕ^* parameters agree well to within their errors. The need for a second Schechter component in the r band is less evident than at longer wavelengths; however, its effects in causing a steeper drop-off at the bright end can clearly be seen in improving the fit to the data.

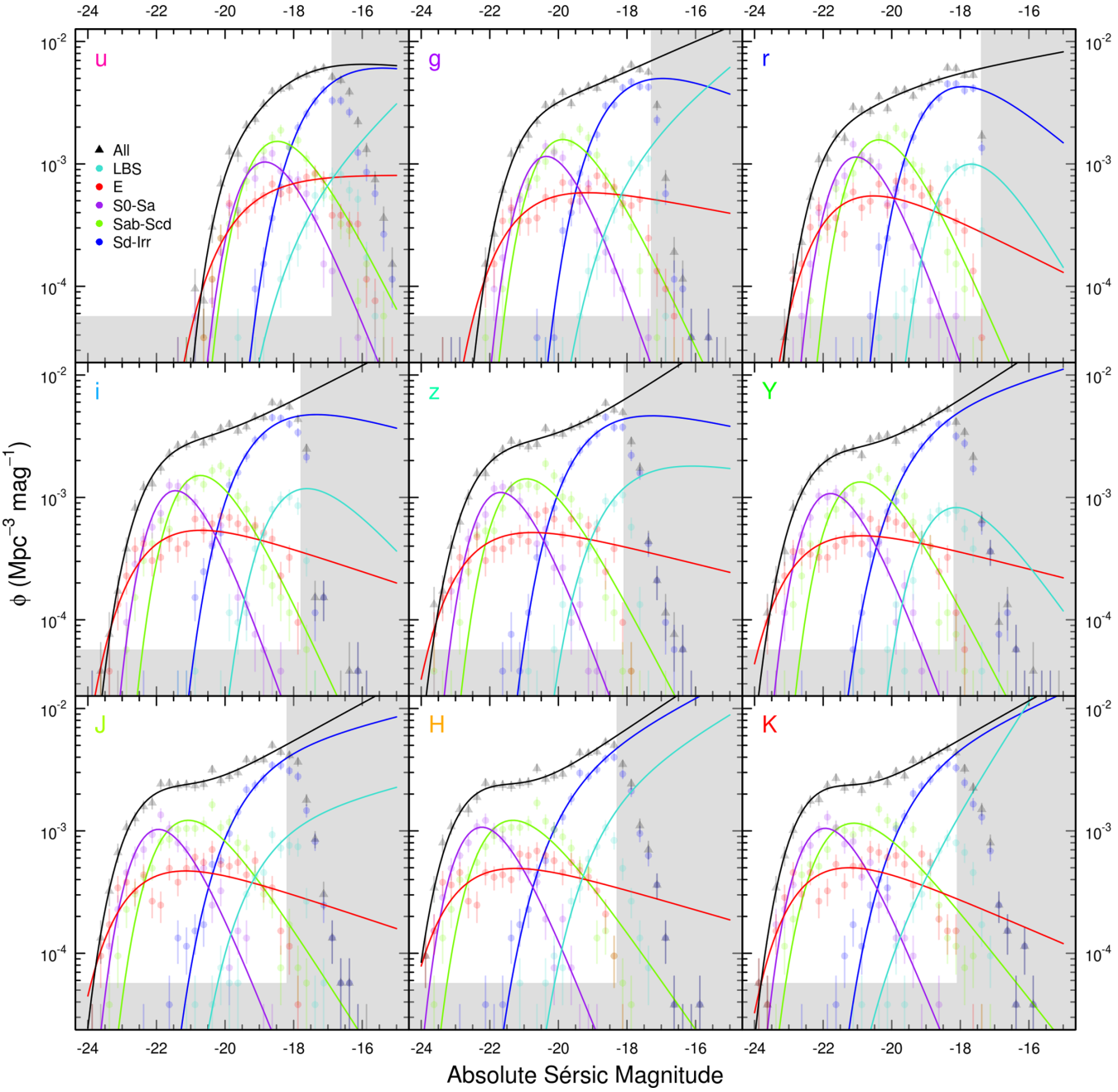

Figure 10. MLFs across all nine bands for the various morphological types (coloured points and lines, as indicated) and total populations (black points and lines). Each morphological population has been fitted with a single-Schechter function and is identical to those shown in Fig. 8. Total populations have been fitted with a double-Schechter function. Prior to fitting, the data are split into bins of 0.25 mag, with the error on the measurement per bin taken as Poissonian ($\sqrt{n}$) in nature. Shaded grey areas indicate those regions where data have not been used in the fits. Variable faint-end magnitude limits are given in Table 2. The additional Schechter function for the total population allows for the notable upturn at faint magnitudes to be properly accounted for, especially at longer wavelengths.

6 THE CSED BY HUBBLE TYPE

The morphological classifications derived in Section 3 are useful for many purposes beyond measuring the luminosity distributions listed in Tables 3–9. One in particular is the sub-division of the CSED (Hill et al. 2010)[10] by morphological type. The CSED can be derived from the fitted LFs, or directly by summing the flux from a volume-limited galaxy sample observed across a broad wavelength range (see Driver et al. 2012 for a discussion of the two methods, with the latter generally being favoured if the data are sufficiently

[10] The CSED is distinct to the energy in photons within a fixed volume (see for example Domínguez et al. 2011), as the majority of these were generated at earlier epochs (i.e. the CSED is the instantaneous energy production rate whereas the extragalactic background light is the integrated energy production incorporating cosmological effects).

Table 9. Double-Schechter LF fit parameters for the total GLF as shown in Fig. 10. From left to right, columns are GAMA passband; the shared knee in the Schechter function (M^*); the primary slope of the faint end of the Schechter function (α_1); the primary normalization constant of the Schechter function (ϕ_1^*); the secondary slope of the faint end of the Schechter function (α_2); the secondary normalization constant of the Schechter function (ϕ_2^*); the χ^2 goodness of fit parameter (χ^2/ν); and the luminosity density (j). Errors are estimated from jackknifed resampling using the relation $\sigma^2 = \frac{N-1}{N}\sum_{i=1}^{N}\left(x_j - x\right)^2$, where x is the best-fitting parameter, x_j is the best-fitting parameter as given from a jackknife resampled variant of the data set and N is the number of jackknife volumes. We adopt $N = 10$.

Band	M^* (mag)	α_1	$\phi_1^*/10^{-3}$ (mag^{-1} Mpc^{-3})	α_2	$\phi_2^*/10^{-3}$ (mag^{-1} Mpc^{-3})	χ^2/ν	$j/10^7$ (L$_\odot$ Mpc^{-3})
u	-18.53 ± 1.25	-0.91 ± 7.17	9.64 ± 12.91	1.25 ± 6.01	1.46 ± 9.39	1.23	$11.88^{+2.04}_{-2.04}$
g	-20.28 ± 0.26	-1.29 ± 0.14	3.51 ± 1.75	0.06 ± 0.59	4.88 ± 1.22	1.43	$14.16^{+0.58}_{-0.58}$
r	-20.90 ± 0.26	-1.13 ± 0.07	4.51 ± 1.03	0.53 ± 0.56	3.01 ± 0.83	2.71	$15.84^{+0.71}_{-0.71}$
i	-21.45 ± 0.20	-1.35 ± 0.21	2.20 ± 1.50	-0.09 ± 0.48	4.87 ± 1.34	1.41	$19.75^{+0.85}_{-0.85}$
z	-21.78 ± 0.25	-1.46 ± 0.21	1.40 ± 1.12	-0.26 ± 0.44	5.05 ± 0.88	1.25	$23.31^{+1.36}_{-1.36}$
Y	-21.76 ± 0.24	-1.45 ± 0.23	1.44 ± 1.25	-0.10 ± 0.54	4.83 ± 0.84	0.68	$22.67^{+1.09}_{-1.09}$
J	-21.82 ± 0.17	-1.38 ± 0.13	1.58 ± 0.76	0.08 ± 0.35	4.78 ± 0.72	1.27	$26.00^{+1.36}_{-1.36}$
H	-22.04 ± 0.26	-1.46 ± 2.43	1.35 ± 6.33	0.08 ± 2.58	5.30 ± 6.69	1.21	$38.78^{+3.01}_{-3.01}$
K	-21.72 ± 0.23	-1.39 ± 1.62	1.64 ± 3.13	0.24 ± 1.55	5.09 ± 3.18	0.86	$47.13^{+3.10}_{-3.10}$

deep). The CSED describes the instantaneous attenuated energy production rate of the Universe today. The energy budget, like the mass budget, is a fundamental description of the Universe which can be readily compared to complex (e.g. Somerville et al. 2012) or basic (e.g. Driver et al. 2013) model prescriptions.

At the present epoch, the energy production budget is almost entirely dominated and driven by stellar nucleosynthesis combined with dust reprocessing of the emergent starlight (i.e. the AGN contribution at very low redshift is negligible; see Driver et al. 2012). Because of the latter effect, the CSED comes in two flavours, attenuated (i.e. as observed) and unattenuated (i.e. dust corrected), both of which are useful. For example to measure the global SFR of a specific sub-population, one desires the unattenuated CSED, but to quantify the ambient intergalactic UV flux one requires the attenuated CSED.

While the attenuated CSED is straightforward to derive, the unattenuated CSED requires a correction for the wavelength- and inclination-dependent photon escape fraction. The FUV to K photon escape fraction, integrated over all inclinations for the zero-redshift galaxy population, was recently quantified by Driver et al. (2007, 2008) using data from the Millennium Galaxy Catalogue (MGC; Liske et al. 2003; Driver et al. 2005). Here the MGC data were used to constrain the face-on central opacity ($\tau_B \sim 3.8$) of the disc galaxy population (Driver et al. 2007) by comparison of the inclination-dependent $B_{\rm MGC}$-band M^* value, with predictions from the detailed radiative transfer modelling described in Popescu et al. 2011 (see also Popescu et al. 2000 and Tuffs et al. 2004). It is worth noting that this dust prescription incorporates full radiative transfer treatment including anisotropic scattering processes from within three distinct dust components: an extended optically thin double-exponential dust disc, a compact optically thick double-exponential dust disc and clumpy components associated with star-forming complexes, with a prescription that allows for cloud fragmentation (Tuffs et al. 2004).

Here we report the contribution of each morphological type to both the attenuated and unattenuated CSED using the photon escape fraction described above for the S(B)ab-S(B)cd, Sd-Irr and LBS populations, and assuming that the E and S(B)0-S(B)a populations are dust free. We opt to dust correct LBS galaxies after a non-exhaustive examination of the spectra of a large number of these systems wherein we found repeated evidence for ongoing star formation. While Sa galaxies in our sample may indeed contain dust, we assume that to first order a correction of this type is broadly correct. Note that Rowlands et al. (2012) recently showed from *Herschel*-ATLAS data that at most 10 per cent of the elliptical population contains dust (see also Agius et al. 2013). In due course the variation of dust properties with morphological type will be investigated using the FUV to far-IR GAMA multiwavelength data set (see Driver et al., in preparation).

6.1 Measuring the integrated fluxes

Any description of the CSED will be incomplete without the inclusion of FUV and NUV estimates. This is because almost 40 per cent of the energy of a global population emerges at wavelengths below 400 nm (Driver et al. 2012). Rather than computing the full Sérsic LFs as we have done in the *ugrizYJHK* bands, here we simply elect to sum the FUV and NUV flux for the distinct samples directly and divide by the volume probed. Our FUV and NUV data are taken from the *GALEX* satellite, specifically a combination of Medium Imaging Survey (MIS) archival and proprietary data obtained by the MIS and GAMA teams (see Driver et al. 2012 for further details).

Table 10 shows the luminosity density values derived directly by summing the fluxes of all systems within our volume and for each population. Only galaxies which lie in the common region (i.e. sampled by all 11 bands; see Driver et al. 2012) are included and the volume is modified accordingly to compensate ($\times$ 0.86). The luminosity densities shown in Table 10 can be compared to those derived from the fitted Schechter functions in Tables 3–9. As discussed in Driver et al. (2012), discrepancies between these two estimates can arise from the extrapolation of the fitted Schechter function combined with sub-optimal fits around the L^* region. The sum of these values for the individual morphological classes also agrees well with the global values reported in Driver et al. (2012), implying internal consistency between the various GAMA sub-samples and methodologies. In detail the FUV and NUV values reported here are lower which is also consistent with the slightly lower median redshift given the steeply declining cosmic star formation history (see for example Hopkins & Beacom 2006; Driver et al. 2013) – i.e.

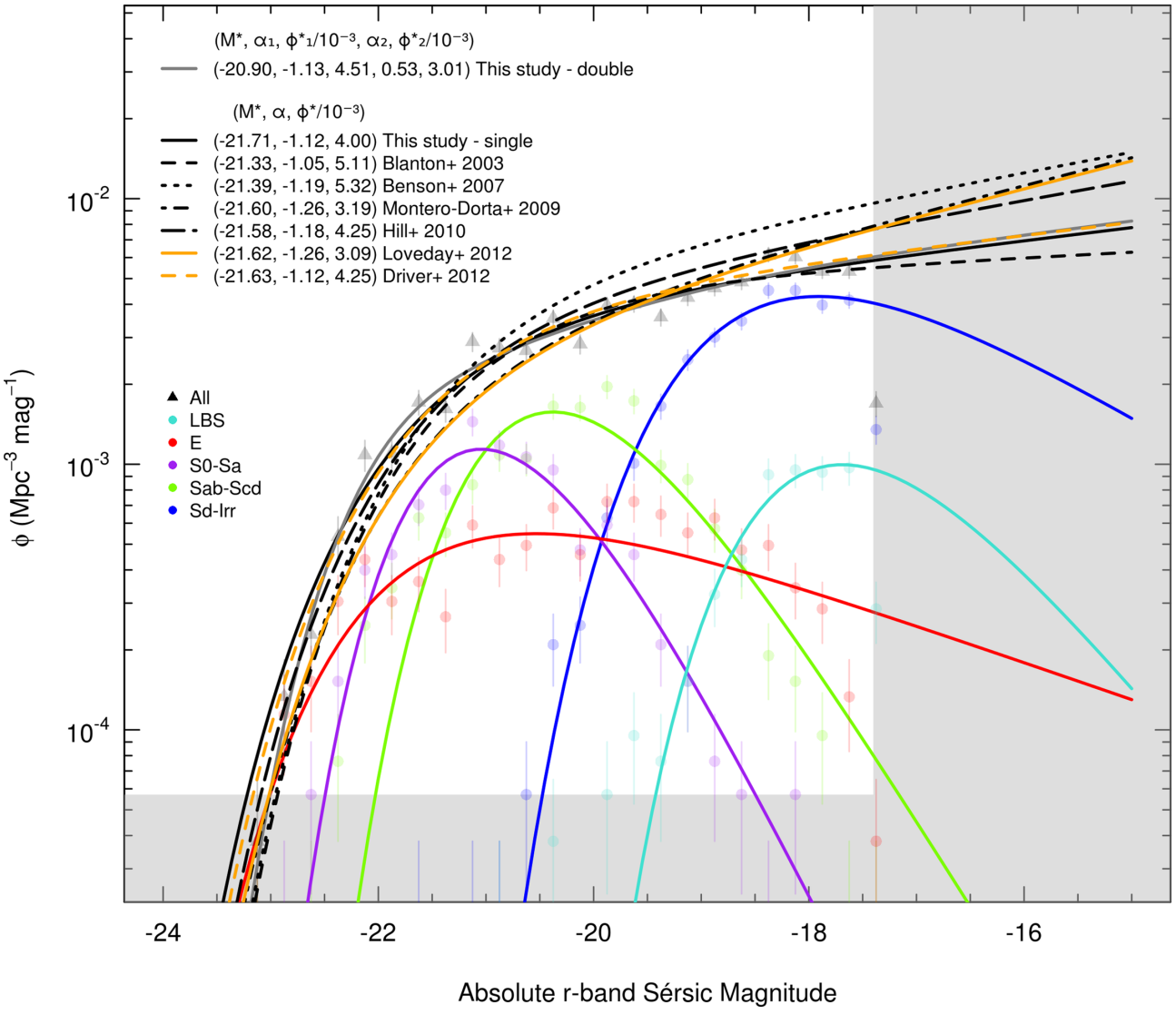

Figure 11. MLFs in the *r* band fitted by single-Schechter functions in addition to the total LF fitted by both a single- and double-Schechter function, shown in grey and black, respectively. Each morphology is labelled and coloured according to the inset legend. Prior to fitting, the data are split into bins of 0.25 mag, with the error per bin assumed as Poissonian ($\sqrt{n}$) in nature. Shaded grey areas ($M > -17.4$ mag and $n \leq 3$) indicate those regions where data have not been used in constraining the Schechter fits. Schechter fit parameters from the global fits (inset, top left) in addition to single-Schechter fits from other studies are also shown, for reference. Where appropriate, Schechter fit data from other studies have been *k*-corrected from $z = 0.1$ back to a $z = 0$ rest frame using a typical correction of $k_{0.1} = 0.12$. Blanton et al. (2003), Montero-Dorta & Prada (2009) and Loveday et al. (2012) have been corrected in this fashion, whereas Benson, Džanović, Frenk & Sharples (2007), Hill et al. (2010) and Driver et al. (2012) have not. Note that the Benson et al. (2007) values have been scaled up by a factor of 10.

$z \sim 0.04$ versus $z \sim 0.08$, equivalent to a time interval of ∼0.5 Gyr. Note that, from Driver et al. (2013), we expect the mean cosmic SFR at $z = 0.06$ to be ∼22 per cent higher than at $z = 0$.

6.2 SFRs by morphological type

The dust-corrected FUV luminosity density can be converted directly to a measure of the SFR. These values are shown in Table 11 and assume a photon escape fraction of 23 per cent. In brief, this photon escape fraction is determined by deriving the GLF in the *B* band for galaxies taken from the MGC (Liske et al. 2003), subdivided by inclination. The trends in M^* with cos (*i*) are compared to those predicted by the complex dust models of Tuffs et al. (2004) (see also Popescu et al. 2011), and used to constrain the face-on central opacity (Driver et al. 2007). In Driver et al. (2008), this value is used to predict the average photon escape fraction as a function of wavelength (see table 3 of Driver et al. 2012). We use the standard prescription by Kennicutt (1989) to derive the SFR which is based on a Salpeter (1955) initial mass function. The values reported in Table 11 are typically two times higher than those reported by James et al. (2008, see their fig. 7). As no evolutionary corrections to the magnitudes are applied, these values correspond to a measurement of the SFR at the median redshift of $z \sim 0.04$ (again, a ∼0.5 Gyr time interval). Additionally, our 'All' measurement is approximately two times lower than that reported in Robotham & Driver (2011), which is again consistent when taking into account the median redshift offset between these two data sets. Our data also confirm the trend seen by James et al. (2008), that the SFR density in the nearby

Table 10. Luminosity densities as a function of wavelength and morphological type.

Wavelength band	(μm)	Hubble type All	E	S(B)0-S(B)a	S(B)ab-S(B)cd	Sd-Irr	LBS
		(10^7 $L_\odot$ Mpc^{-3})					
FUV	0.153	16 378.14 ± 2504.93	699.05 ± 106.91	1928.87 ± 295.01	7069.65 ± 1081.25	3010.56 ± 460.44	380.42 ± 58.18
NUV	0.230	115.64 ± 17.69	7.30 ± 1.12	15.56 ± 2.38	49.45 ± 7.56	19.95 ± 3.05	2.48 ± 0.38
u	0.355	11.93 ± 0.95	1.95 ± 0.16	2.53 ± 0.20	4.44 ± 0.36	1.45 ± 0.12	0.17 ± 0.01
g	0.467	12.56 ± 1.01	2.78 ± 0.22	3.30 ± 0.26	4.11 ± 0.33	1.25 ± 0.10	0.14 ± 0.01
r	0.616	15.13 ± 1.21	3.77 ± 0.30	4.32 ± 0.35	4.64 ± 0.37	1.33 ± 0.11	0.15 ± 0.01
i	0.747	18.05 ± 1.44	4.68 ± 0.37	5.32 ± 0.43	5.45 ± 0.44	1.49 ± 0.12	0.16 ± 0.01
z	0.892	21.54 ± 1.72	5.83 ± 0.47	6.66 ± 0.53	6.22 ± 0.50	1.61 ± 0.13	0.18 ± 0.01
Y	1.030	22.06 ± 1.76	6.05 ± 0.48	7.08 ± 0.57	6.24 ± 0.50	1.56 ± 0.12	0.18 ± 0.01
J	1.248	25.80 ± 2.06	7.10 ± 0.57	8.56 ± 0.68	7.32 ± 0.59	1.61 ± 0.13	0.20 ± 0.02
H	1.631	38.41 ± 3.07	10.65 ± 0.85	12.88 ± 1.03	10.80 ± 0.86	2.46 ± 0.20	0.27 ± 0.02
K	2.201	45.60 ± 3.65	12.47 ± 1.00	15.40 ± 1.23	12.95 ± 1.04	2.88 ± 0.23	0.32 ± 0.03

Table 11. The SFR density for each morphological type as derived from the FUV luminosity densities reported in Table 10.

Hubble type	SFR ($M_\odot$ yr^{-1} Mpc^{-3})	SFR contribution (per cent)
All	0.0125 ± 0.0030	100
E	0.0001 ± 0.0001	1
S(B)0-S(B)a	0.0020 ± 0.0003	16
S(B)ab-S(B)cd	0.0073 ± 0.0011	58
Sd-Irr	0.0031 ± 0.0005	25
LBS	<0.0001 ± 0.0001	<1

Universe is dominated by the intermediate S(B)ab-S(B)cd Hubble types, with a sharp decline towards earlier or later types.

6.3 The attenuated CSED

Fig. 12 shows the full FUV to *K* attenuated CSED (i.e. as observed) for each of the populations. Overlaid as black data points is the global CSED reported in Driver et al. (2012) derived for the full GAMA $z < 0.1$ sample. Note that the earlier data include the sample variance uncertainty indicated by the error bars and dotted uncertainty ranges. As here we are interested in the variations between the morphological types within a single volume, we do not include the cosmic variance errors. For each morphological type, we fit a range of single stellar population (SSP) PEGASE models (see Fioc & Rocca-Volmerange 1999) to our data. The best fits are shown in Fig. 12 by the colour indicated in the key. The sum of these fits is shown as the black curve which agrees well with the $z < 0.1$ CSED showing only a slight discrepancy in the UV where one might expect a slightly reduced CSED due to the declining SFR from $z = 0.08$ to 0.04 (i.e. $\Delta t \sim 0.5$ Gyr). We do not report the PEGASE values for these curves as they are simply being used here as appropriate fitting functions. Integrating these functions therefore provides a direct measure of the instantaneous energy production emerging from each galaxy population. The total energy output is (8.53 ± 0.20) × 10^{34} W Mpc^{-3} with approximate sub-divisions of 27, 31, 32, 9 and 1 per cent arising from the E, S(B)0-S(B)a, S(B)ab-S(B)cd, Sd-Irr and LBS populations, respectively. This is surprisingly well balanced and shows that all galaxy types contribute significantly to the ambient intergalactic radiation field, i.e. ∼58 per cent spheroid dominated and ∼42 per cent disc dominated.

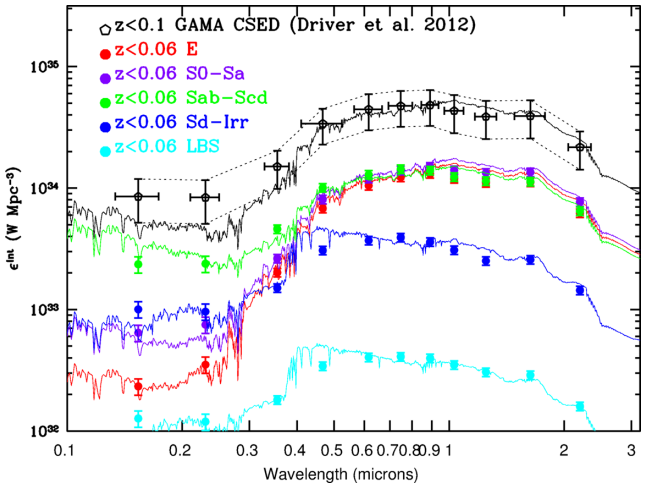

Figure 12. The attenuated (as observed) CSED. Integration under each line provides a direct measure of the emergent observed instantaneous energy production for each galaxy population.

6.4 The unattenuated CSED

Fig. 13 shows the unattenuated (corrected) CSED for each of the populations by applying the photon escape fraction prescription determined in Driver et al. (2008) to the S(B)ab-S(B)cd, Sd-Irr and LBS populations only. Similarly these data are fitted to a range of PEGASE SSP model as before and integrated to give the instantaneous energy production of (1.12 ± 0.15) × 10^{35} W Mpc^{-3} approximately sub-divided by 21, 23, 44, 11 and 1 per cent for the E, S(B)0-S(B)a, S(B)ab-S(B)cd, Sd-Irr and LBS populations, respectively. Hence, we see that although the energy which enters into the intergalactic medium is dominated 58:42 by spheroid-dominated:disc-dominated types, the actual energy production rate is almost inverted, i.e. 44:56 spheroid-dominated:disc-dominated.

7 CONCLUSIONS

We have defined a local ($0.025 < z < 0.06$) volume-limited sample of 3727 galaxies (GAMAnear) taken from the GAMA survey (Driver et al. 2009). Using GAMA-reprocessed nine-band imaging from the SDSS (*ugriz*; York et al. 2000; Abazajian et al. 2009)

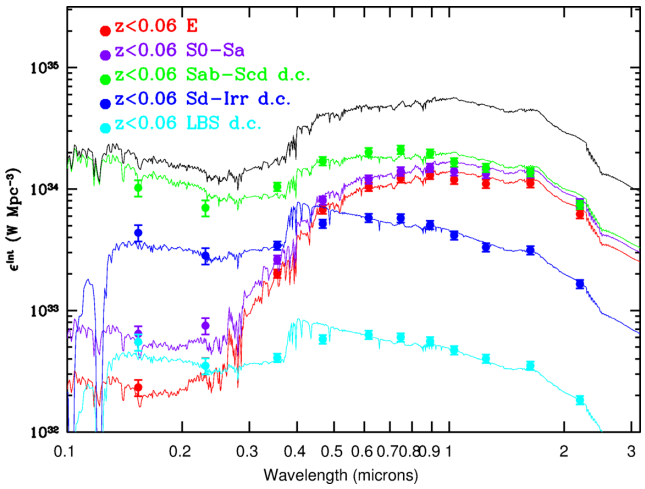

Figure 13. The unattenuated (corrected) CSED. Integration under each line provides a direct measure of the emergent corrected instantaneous energy production for each galaxy population.

and UKIDSS-LAS (*YJHK*; Lawrence et al. 2007) surveys, we provide robust visual classifications for each galaxy in our sample into its morphological Hubble type [E, S(B)0-S(B)a, S(B)ab-S(B)cd, Sd-Irr], alongside an additional LBS class, a class of potential blue dwarf ellipticals and a contaminant 'star' class. Approximately 27 per cent of this sample is visually classified as spheroid dominated, with the remaining ∼73 per cent visually classified as disc dominated or LBS. We explore morphological trends with several global measurements, namely *r*-band half-light radius (kpc); ellipticity as measured in the *r* band, absolute *r*-band Sérsic magnitude (truncated at 10 r_e); rest-frame $(u - r)$ colour; and *r*-band Sérsic index. In these global parameter spaces, we are able to reproduce several well-known morphological relations, including the curved magnitude–radius relation for elliptical galaxies (Forbes et al. 2008; Graham & Worley 2008) and the galaxy population bimodality as has been shown in, e.g., Baldry et al. (2004), Driver et al. (2006) and Kelvin et al. (2012).

Using GAMA single-Sérsic (Sérsic 1963, 1968) structural measurements (Kelvin et al. 2012), we maintain that the most meaningful measurement of the total flux of a galaxy is that given by the Sérsic magnitude, truncated at 10 multiples of the half-light radius. This estimate of total flux allows us to derive LFs for both the global population and the constituent morphology sub-populations in each passband (*ugrizYJHK*). We confirm that the total GLF is best described by a double-Schechter form (Schechter 1976) with a single distinctive 'knee' (L^*/M^*) parameter. Conversely, we find that the constituent MLFs are well described by a single-Schechter form. Tables 3–9 provide full Schechter fit parameters for these data across all nine wavelengths.

Our morphological classifications allow for the division of the CSED by morphological type. The CSED describes the instantaneous energy production rate of the Universe, providing a means by which cosmological model predictions of the total local energy budget may be tested. Here we provide estimates of the CSED by directly summing the flux in our volume-limited sample for each morphological type across each wavelength. Note that we include flux measurements from the FUV and NUV in order to account for the significant energy contribution at wavelengths below 400 nm. The energy production budget today is mainly comprised of both stellar nucleosynthesis and dust reprocessing. Therefore, we have measured both the attenuated (i.e. as observed) and unattenuated (i.e. dust-corrected) CSEDs for each morphological type by fitting a series of SSP PEGASE models (Fioc & Rocca-Volmerange 1999) to each population.

Based on our dust-corrected FUV flux estimates, we also construct estimates of the local ($z \sim 0.04$) SFR density sub-divided by morphology. We find the SFR density across this redshift range to be dominated by the intermediate S(B)ab-S(B)cd morphological-type systems, declining sharply at earlier or later Hubble types, and confirming the trend seen in James et al. (2008).

In addition, we find that ∼58 per cent of the total attenuated (observed) energy output in the local Universe emerges from spheroid-dominated galaxies, with the remaining ∼42 per cent found in disc-dominated systems. The summation of these fits gives a total observed energy output of $(8.53 \pm 0.20) \times 10^{34}$ W Mpc^{-3}, in good agreement with that of Driver et al. (2012). The unattenuated CSEDs are derived by applying the photon escape fraction prescription detailed in Driver et al. (2008), calibrated using the radiative transfer models of Popescu et al. (2011), to the S(B)ab-S(B)cd, Sd-Irr and LBS populations only. We find that ∼44 per cent of the total unattenuated (corrected) energy output in the local Universe emerges from spheroid-dominated galaxies, with the remaining ∼56 per cent found in disc-dominated systems. The summation of these fits gives a total corrected energy output in the local Universe of $(1.12 \pm 0.15) \times 10^{35}$ W Mpc^{-3}.

ACKNOWLEDGEMENTS

This work was supported by the Austrian Science Foundation FWF under grant P23946. AWG was supported under the Australian Research Council's funding scheme FT110100263. GAMA is a joint European–Australasian project based around a spectroscopic campaign using the Anglo-Australian Telescope. The GAMA input catalogue is based on data taken from the Sloan Digital Sky Survey and the UKIRT Infrared Deep Sky Survey. Complementary imaging of the GAMA regions is being obtained by a number of independent survey programmes including *GALEX* MIS, VST KiDS, VISTA VIKING, *WISE*, *Herschel*-ATLAS, GMRT and ASKAP providing UV to radio coverage. GAMA is funded by the STFC (UK), the ARC (Australia), the AAO and the participating institutions. The GAMA website is http://www.gama-survey.org/.

REFERENCES

Abazajian K. N. et al., 2009, ApJS, 182, 543
Agius N. K. et al., 2013, MNRAS, 431, 1929
Allen P. D., Driver S. P., Graham A. W., Cameron E., Liske J., de Propris R., 2006, MNRAS, 371, 2
Arp H., 1965, ApJ, 142, 402
Baldry I. K., Glazebrook K., Brinkmann J., Ivezić Ž., Lupton R. H., Nichol R. C., Szalay A. S., 2004, ApJ, 600, 681
Baldry I. K. et al., 2010, MNRAS, 404, 86
Baldry I. K. et al., 2012, MNRAS, 421, 621
Bamford S. P. et al., 2009, MNRAS, 393, 1324
Bauer A. E. et al., 2013, MNRAS, 434, 209
Benson A. J., Džanović D., Frenk C. S., Sharples R., 2007, MNRAS, 379, 841
Bertin E., 2011, in Evans I. N., Accomazzi A., Mink D. J., Rots A. H., eds, ASP Conf. Ser. Vol. 442, Astronomical Data Analysis Software and Systems XX. Astron. Soc. Pac., San Francisco, p. 435
Bertin E., Arnouts S., 1996, A&AS, 117, 393
Binggeli B., Sandage A., Tarenghi M., 1984, AJ, 89, 64
Blanton M. R. et al., 2003, ApJ, 592, 819

Brough S. et al., 2011, MNRAS, 413, 1236
Cameron E., 2011, Publ. Astron. Soc. Aust., 28, 128
Caon N., Capaccioli M., Rampazzo R., 1990, A&AS, 86, 429
Caon N., Capaccioli M., D'Onofrio M., 1993, MNRAS, 265, 1013
Caon N., Capaccioli M., D'Onofrio M., 1994, A&AS, 106, 199
Capaccioli M., 1989, in Corwin H. G., Jr, Bottinelli L., eds, World of Galaxies (Le Monde des Galaxies). Springer-Verlag, New York, p. 208
Cappellari M. et al., 2011, MNRAS, 413, 813
Carollo C. M. et al., 2013, ApJ, 773, 112
Carter D., 1978, MNRAS, 182, 797
Carter D., 1987, ApJ, 312, 514
Ciotti L., 1991, A&A, 249, 99
Conselice C. J., 2006, MNRAS, 373, 1389
Davies R. L., Efstathiou G., Fall S. M., Illingworth G., Schechter P. L., 1983, ApJ, 266, 41
de Vaucouleurs G., 1948, Ann. Astrophys., 11, 247
Debattista V. P., Mayer L., Carollo C. M., Moore B., Wadsley J., Quinn T., 2006, ApJ, 645, 209
Diaferio A., Kauffmann G., Balogh M. L., White S. D. M., Schade D., Ellingson E., 2001, MNRAS, 323, 999
Domínguez A. et al., 2011, MNRAS, 410, 2556
Dressler A., 1980, ApJ, 236, 351
Driver S. P., 1999, ApJ, 526, L69
Driver S. P., Liske J., Cross N. J. G., De Propris R., Allen P. D., 2005, MNRAS, 360, 81
Driver S. P. et al., 2006, MNRAS, 368, 414
Driver S. P., Popescu C. C., Tuffs R. J., Liske J., Graham A. W., Allen P. D., de Propris R., 2007, MNRAS, 379, 1022
Driver S. P., Popescu C. C., Tuffs R. J., Graham A. W., Liske J., Baldry I., 2008, ApJ, 678, L101
Driver S. P. et al., 2009, Astron. Geophys., 50, 050000
Driver S. P. et al., 2011, MNRAS, 413, 971
Driver S. P. et al., 2012, MNRAS, 427, 3244
Driver S. P., Robotham A. S. G., Bland-Hawthorn J., Brown M., Hopkins A., Liske J., Phillipps S., Wilkins S., 2013, MNRAS, 430, 2622
Drory N., Fisher D. B., 2007, ApJ, 664, 640
Erwin P., Beltrán J. C. V., Graham A. W., Beckman J. E., 2003, ApJ, 597, 929
Fioc M., Rocca-Volmerange B., 1999, preprint (astro-ph/9912179)
Forbes D. A., Lasky P., Graham A. W., Spitler L., 2008, MNRAS, 389, 1924
Gadotti D. A., 2009, MNRAS, 393, 1531
Graham A. W., 2013, in Oswalt T. D., Keel W. C., eds, Planets, Stars and Stellar Systems, Vol. 6. Springer, Dordrecht, p. 91
Graham A. W., Driver S. P., 2005, Publ. Astron. Soc. Aust., 22, 118
Graham A. W., Worley C. C., 2008, MNRAS, 388, 1708
Graham A. W., Driver S. P., Petrosian V., Conselice C. J., Bershady M. A., Crawford S. M., Goto T., 2005, AJ, 130, 1535
Gunn J. E., Gott J. R., III, 1972, ApJ, 176, 1
Guzman R., Gallego J., Koo D. C., Phillips A. C., Lowenthal J. D., Faber S. M., Illingworth G. D., Vogt N. P., 1997, ApJ, 489, 559
Hill D. T., Driver S. P., Cameron E., Cross N., Liske J., Robotham A., 2010, MNRAS, 404, 1215
Hill D. T. et al., 2011, MNRAS, 412, 765
Holmberg E., 1958, Meddelanden fran Lunds Astron. Obs. Ser. II, 136, 1
Hopkins A. M., Beacom J. F., 2006, ApJ, 651, 142
Hopkins A. M. et al., 2013, MNRAS, 430, 2047
Hubble E. P., 1926, ApJ, 64, 321
Hubble E. P., 1936, Realm of the Nebulae. Yale University Press, New Haven
James P. A., Knapen J. H., Shane N. S., Baldry I. K., de Jong R. S., 2008, A&A, 482, 507
Jeans J. H., 1919, Problems of Cosmogony and Stellar Dynamics. Cambridge Univ. Press, Cambridge
Kauffmann G., White S. D. M., Guiderdoni B., 1993, MNRAS, 264, 201
Kelvin L. S. et al., 2012, MNRAS, 421, 1007
Kennicutt R. C., Jr, 1989, ApJ, 344, 685
Kormendy J., Bender R., 1996, ApJ, 464, L119
Kormendy J., Bender R., 2012, ApJS, 198, 2
Larson R. B., Tinsley B. M., Caldwell C. N., 1980, ApJ, 237, 692
Laurikainen E., Salo H., Buta R., Knapen J. H., Comerón S., 2010, MNRAS, 405, 1089
Lawrence A. et al., 2007, MNRAS, 379, 1599
Lintott C. J. et al., 2008, MNRAS, 389, 1179
Lintott C. et al., 2011, MNRAS, 410, 166
Liske J., Lemon D. J., Driver S. P., Cross N. J. G., Couch W. J., 2003, MNRAS, 344, 307
Loveday J. et al., 2012, MNRAS, 420, 1239
Misgeld I., Hilker M., 2011, MNRAS, 414, 3699
Montero-Dorta A. D., Prada F., 2009, MNRAS, 399, 1106
Moore B., Katz N., Lake G., Dressler A., Oemler A., 1996, Nature, 379, 613
Nair P. B., Abraham R. G., 2010, ApJS, 186, 427
Navarro J. F., Benz W., 1991, ApJ, 380, 320
Park C., Gott J. R., III, Choi Y.-Y., 2008, ApJ, 674, 784
Pastrav B. A., Popescu C. C., Tuffs R. J., Sansom A. E., 2013a, A&A, 553, A80
Pastrav B. A., Popescu C. C., Tuffs R. J., Sansom A. E., 2013b, A&A, 557, A137
Peng C. Y., Ho L. C., Impey C. D., Rix H.-W., 2010, AJ, 139, 2097
Phillipps S., Driver S., 1995, MNRAS, 274, 832
Pimbblet K. A., Jensen P. C., 2012, MNRAS, 426, 1632
Popescu C. C., Misiriotis A., Kylafis N. D., Tuffs R. J., Fischera J., 2000, A&A, 362, 138
Popescu C. C., Tuffs R. J., Dopita M. A., Fischera J., Kylafis N. D., Madore B. F., 2011, A&A, 527, A109
Popesso P., Biviano A., Böhringer H., Romaniello M., 2006, A&A, 445, 29
Prescott M., Baldry I. K., James P. A., 2009, MNRAS, 397, 90
Reynolds J. H., 1920, MNRAS, 80, 746
Robotham A. S. G., Driver S. P., 2011, MNRAS, 413, 2570
Robotham A. et al., 2010, Publ. Astron. Soc. Aust., 27, 76
Robotham A. S. G. et al., 2011, MNRAS, 416, 2640
Rowlands K. et al., 2012, MNRAS, 419, 2545
Saha K., Martinez-Valpuesta I., Gerhard O., 2012, MNRAS, 421, 333
Salpeter E. E., 1955, ApJ, 121, 161
Sandage A., 1961, The Hubble Atlas of Galaxies. Carnegie Institution, Washington
Sandage A., Binggeli B., 1984, AJ, 89, 919
Schechter P., 1976, ApJ, 203, 297
Sérsic J. L., 1963, Bol. Asociacion Argentina Astron. La Plata Argentina, 6, 41
Sérsic J. L., 1968, Atlas de Galaxias Australes. Observatorio Astronomico, Cordoba, Argentina
Shapley H., 1938, Nature, 142, 715
Shapley H., Paraskevopoulos J. S., 1940, Proc. Natl. Acad. Sci., 26, 31
Simard L., Mendel J. T., Patton D. R., Ellison S. L., McConnachie A. W., 2011, ApJS, 196, 11
Somerville R. S., Gilmore R. C., Primack J. R., Domínguez A., 2012, MNRAS, 423, 1992
Steinmetz M., Navarro J. F., 2002, New Astron., 7, 155
Stinson G. S., Dalcanton J. J., Quinn T., Kaufmann T., Wadsley J., 2007, ApJ, 667, 170
Stoughton C. et al., 2002, AJ, 123, 485
Taylor E. N. et al., 2011, MNRAS, 418, 1587
Tuffs R. J., Popescu C. C., Völk H. J., Kylafis N. D., Dopita M. A., 2004, A&A, 419, 821
van den Bergh S., 1976, ApJ, 206, 883
van der Wel A., 2008, ApJ, 675, L13
Wilman D. J., Erwin P., 2012, ApJ, 746, 160
York D. G. et al., 2000, AJ, 120, 1579

APPENDIX A: REDSHIFT LIMITS

Based on prior measurements of structural properties as presented in Allen et al. (2006) and Simard et al. (2011), we calculate the typical physical sizes of bulges and discs in the local Universe. Adopting the redshifts provided in each respective catalogue, we convert their reported bulge and disc angular sizes to physical sizes (in kpc)

in accordance with our preferred cosmology, namely (H_0, Ω_m, Ω_Λ) = (70 km s^{-1} Mpc^{-1}, 0.3, 0.7). An appropriate conversion between exponential disc scalelength (as provided in both catalogues) and half-light radius is achieved using the well-known relation

$$r_e = b^n h, \tag{A1}$$

where h is the disc scalelength, n is the Sérsic index (a measure of the shape of the galaxy light profile; see Section 2.1.1 for further details) and b is a function of n. For $n = 1$, $b^n = 1.678$. We discard those model fits that lie outwith the range $0.1 < B/T < 0.9$, limiting each catalogue to those systems that are not dominated by the flux from a single component. Allen et al. (2006) model fits are to B-band imaging data, whereas Simard et al. (2011) fits are in the SDSS r band. As shown in Kelvin et al. (2012), one expects a variation in observed half-light radii with wavelength. The best-fitting relations for both spheroidal (bulge) and disc components are given by

$$\log r_{e,sph} = -0.304 \log \lambda_{rest} + 1.506 \tag{A2}$$

$$\log r_{e,disc} = -0.189 \log \lambda_{rest} + 1.176, \tag{A3}$$

where λ_{rest} is the rest-frame wavelength. Accordingly, we correct the Allen et al. (2006) half-light radii from the B band (445 nm) to the r band (622 nm). We match both catalogues to the GAMA-I tiling catalogue (version 16) to limit our analyses to galaxies that lie within the GAMA volume, and calculate 3σ-clipped robust mean values for the bulge and disc components in both studies.

We find the typical sizes for bulge components in the local Universe as measured in the r band to be 1.93 ± 1.20 and 3.02 ± 1.65 kpc for Allen and Simard, respectively. We find the typical sizes for the corresponding disc components to be 8.19 ± 3.62 and 8.41 ± 4.45 kpc, for Allen and Simard, respectively.[11] Fig. A1 shows the apparent angular size for structures of these physical sizes at varying redshift. The red (blue) solid (dashed) line represents the apparent angular size for bulges (discs) in the Allen (Simard) data, as indicated. The shaded semi-transparent regions around each line represents the half-sigma scatter in the data. In addition, the horizontal dotted line lies at an angular size of 1.1 arcsec, which corresponds to the typical r-band seeing in SDSS (Kelvin et al. 2012).

For this study, we define an upper redshift limit of $z = 0.06$. This limit is chosen such that the majority of bulges (the limiting structural component) should remain resolvable. A lower limit of $z = 0.025$ is also adopted to avoid low galaxy number densities below this redshift and to ensure that measured redshifts are not dominated by peculiar velocities.

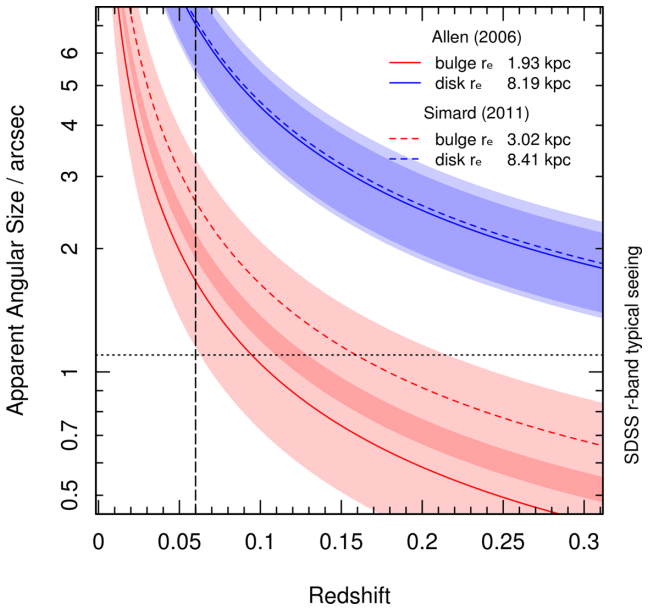

Figure A1. Apparent angular size for typical bulges and discs at varying redshifts. The red (blue) solid (dashed) line represents the apparent angular size for bulges (discs) in the Allen (Simard) data, as indicated. The shaded semi-transparent regions around each line represent the half-sigma scatter in the data. In addition, the horizontal dotted line lies at an angular size of 1.1 arcsec, which corresponds to the typical r-band seeing in SDSS (Kelvin et al. 2012). Our chosen upper redshift limit of $z = 0.06$ is shown as a vertical dashed line.

APPENDIX B: COMPARISON WITH GALAXY ZOO MORPHOLOGIES

To test our visual classifications, we compare our morphological classifications to those of the well-established citizen science project Galaxy Zoo (Lintott et al. 2008). We employ the Galaxy Zoo 1 data release (GZ1; Lintott et al. 2011, table 2) in our analysis below.

GZ1 contains 667 944 sources down to an SDSS apparent magnitude limit of $r = 17.77$ mag for all galaxies in the SDSS Data Release 7 which have spectra included. Of these 667 944 objects, 1779 galaxies exhibit a direct match with the galaxies in our volume-limited GAMAnear sample of 3727 (∼48 per cent) when matching by SDSS object ID (OBJID). Each galaxy in the Galaxy Zoo catalogue is classified as either 'elliptical', 'spiral' or 'uncertain', with an associated probability. We adopt a probability threshold of 80 per cent. A markedly high fraction of this sub-set is classified by Galaxy Zoo as 'uncertain' (1050; 59.0 per cent), with the remainder as 'elliptical' (143; 8.0 per cent) and 'spiral' (586; 32.9 per cent). For comparison, our own matched sub-sample is similarly split into three comparable classification bins: elliptical (324; 18.2 per cent), spiral[12] (S0-Sa→Sd-Irr, 1416; 79.6 per cent) and LBS/star (39; 2.2 per cent).

Fig. B1 shows the cross-correlation results between our own visual classifications and those provided by Galaxy Zoo. The number of galaxies within each bin is shown as 'correlation bubbles', with larger bubbles corresponding to a higher fraction of objects within that bin. The fraction of galaxies within each classification bin is quantified as a percentage of galaxies in our own study (left) and of galaxies from Galaxy Zoo (right). As is shown, the vast majority (99.8 per cent) of the Galaxy Zoo spiral population are also classified as spirals by our method (i.e. the Galaxy Zoo spiral population

[11] Although it is crucial for us to estimate the typical *observed* sizes of bulges and discs in the local Universe when defining appropriate sample redshift limits, we note that due to the effects of dust, projection effects and bulge/disc decomposition considerations, the measured sizes differ from the intrinsic underlying ones. Using the corrections from Pastrav et al. (2013a,b) for $\tau_B^f = 3.8$ (the same average dust opacity used to correct for dust attenuation), we obtain average intrinsic bulge sizes of 1.80 and 2.82 kpc for the Allen and Simard samples, respectively, with corresponding intrinsic disc sizes of 7.00 and 6.19 kpc.

[12] Although lenticular and irregular types exist within this combined population, we label it 'spiral' for brevity and ease of comparison to the Galaxy Zoo data.

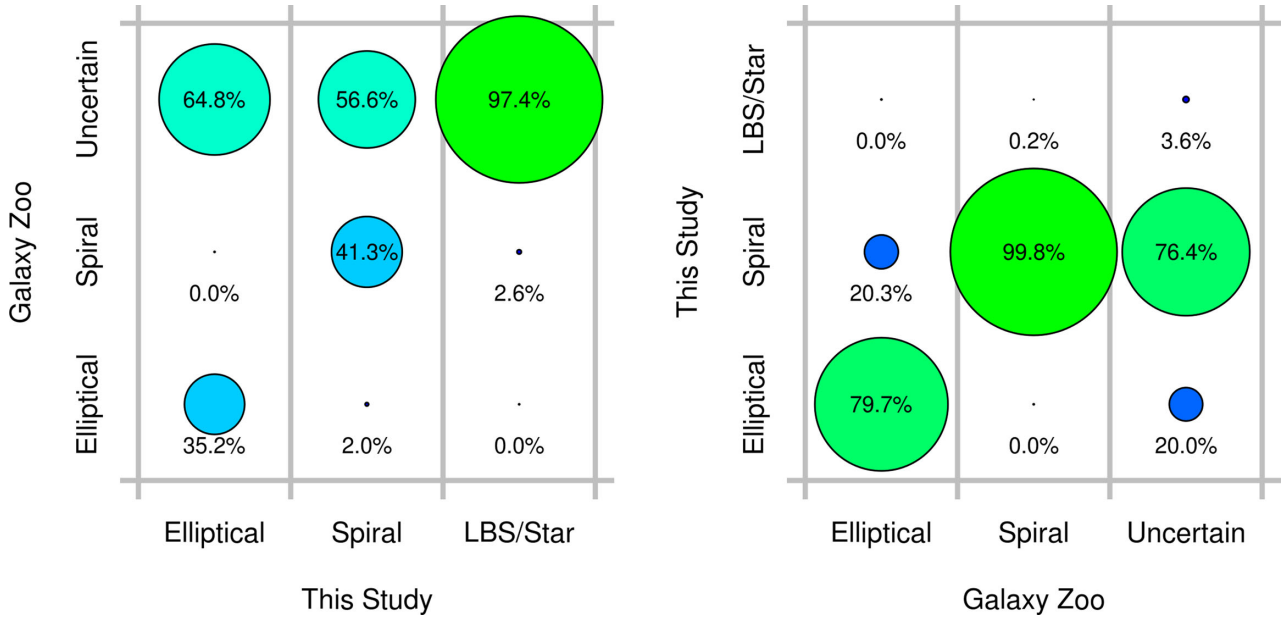

Figure B1. A visual representation of the level of agreement between our visual classifications and those provided by the Galaxy Zoo project (Lintott et al. 2008, 2011). These figures are constructed using a common matched data set of 1779 galaxies from GAMAnear and table 2 of Lintott et al. (2011). Percentages shown depict the fractional agreement with our own classifications (left) and with the Galaxy Zoo classifications (right), that is percentages in any given column total 100 per cent.

is essentially a sub-set of our own), but not all of our spiral galaxies are found to be spiral in the Galaxy Zoo data. A similarly large fraction of the Galaxy Zoo elliptical population (79.7 per cent) are also classified as elliptical by our method, with approximately one fifth of Galaxy Zoo ellipticals classified as spirals in this study. The majority of Galaxy Zoo uncertain galaxies are classified as spiral by our method (76.4 per cent), which may be expected owing to the typically fainter surface brightnesses of galaxies of this type. As is shown in the left-hand panel, more than half of each grouping fall within the Galaxy Zoo uncertain class, almost accounting for the entirety of our LBS/star population. This large Galaxy Zoo uncertain population no doubt arises due to the stringent 80 per cent classification criterion recommended for use in Lintott et al. (2011). We note that the application of a lower 66 per cent threshold (in line with our own classification method) forces a significant fraction of the uncertain population into the two standard 'elliptical' and 'spiral' sub-populations, in good agreement with our own results, albeit with a larger margin of error. Despite the large fraction of uncertain galaxies, we opt to maintain the recommended classification criterion of 80 per cent for our analyses. If one removes the uncertain grouping from this figure, we find that the primary axis (i.e. the [Elliptical, Elliptical]→[Spiral, Spiral] axis) remains strong when using either our own method or Galaxy Zoo as a reference baseline, indicating a good level of agreement between our own classifications and those of Galaxy Zoo.

To summarize, while we acknowledge that Galaxy Zoo morphologies are preferred for studies that require robust morphological information for a large ($>10^5$) number of systems, we advocate that detailed visual inspection by a team of experts produces notable advantages over Galaxy Zoo for small data sets such as that presented in this study. The creation of our own classification scheme has allowed us full control over, for example: classification criteria (and therefore the ultimate resolution on available Hubble types); postage-stamp image creation, including red–green–blue filter selection, image sizes and image scaling (both logarithmic and arctan); and, significantly, our final sample selection. As shown in Fig. B1, we find a good level of agreement in morphological type between those galaxies that exist in both the Galaxy Zoo data set and our own GAMAnear sample. This confirms that our classification scheme is robust and equally applicable to those additional galaxies in our sample that do not have a counterpart in the Galaxy Zoo data base.

APPENDIX C: MORPHOLOGIES IN COLOUR–INDEX SPACE

Below we provide postage-stamp examples of each morphological type as defined in Fig. 3. These types are LBS, Fig. C1; ellipticals, Fig. C2; lenticular/early-type spirals, Fig. C3; barred lenticular/early-type spirals, Fig. C4; late-type spirals, Fig. C5; barred late-type spirals, Fig. C6; and disc-dominated spirals, Fig. C7. Each figure is arranged according to the global K-band Sérsic index and rest-frame $u - r$ colour of the galaxy. Postage-stamp images are created from RGB = *Hig* input data and are approximately 40 arcsec × 40 arcsec in size.

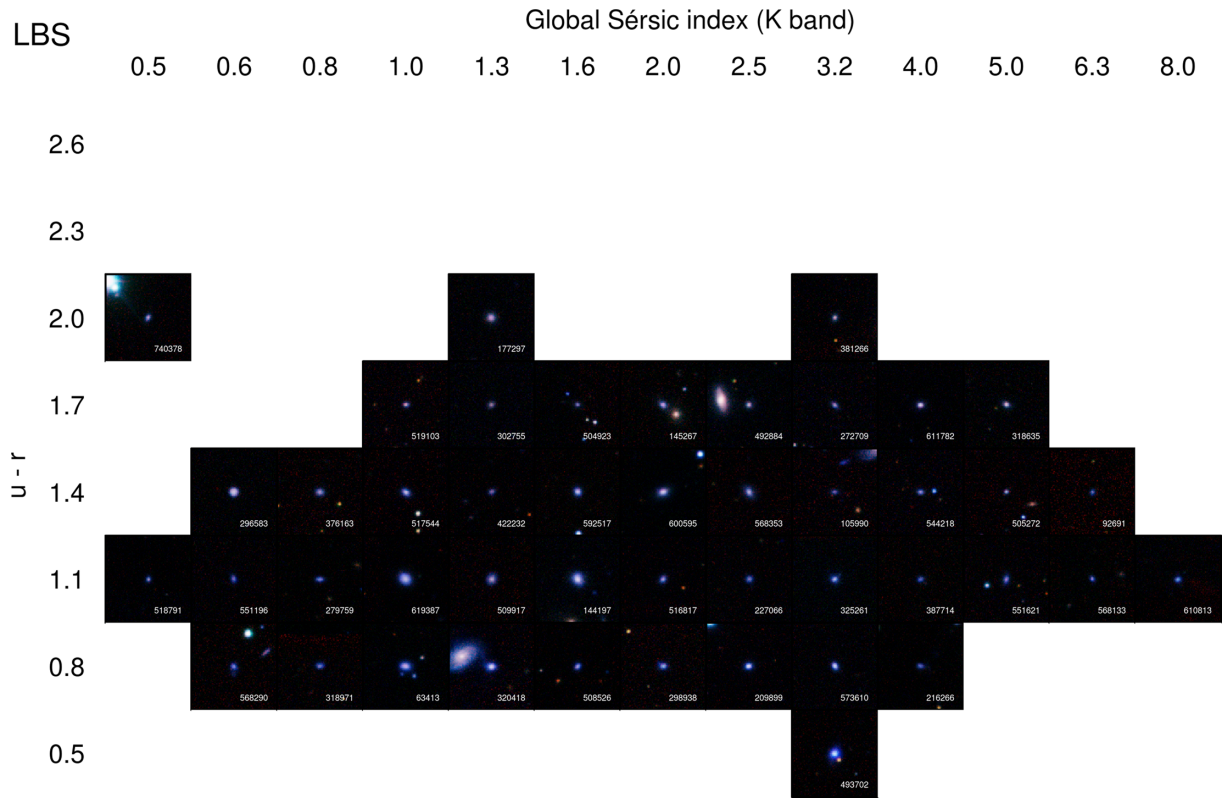

Figure C1. LBS in $u - r$ colour–Sérsic index space.

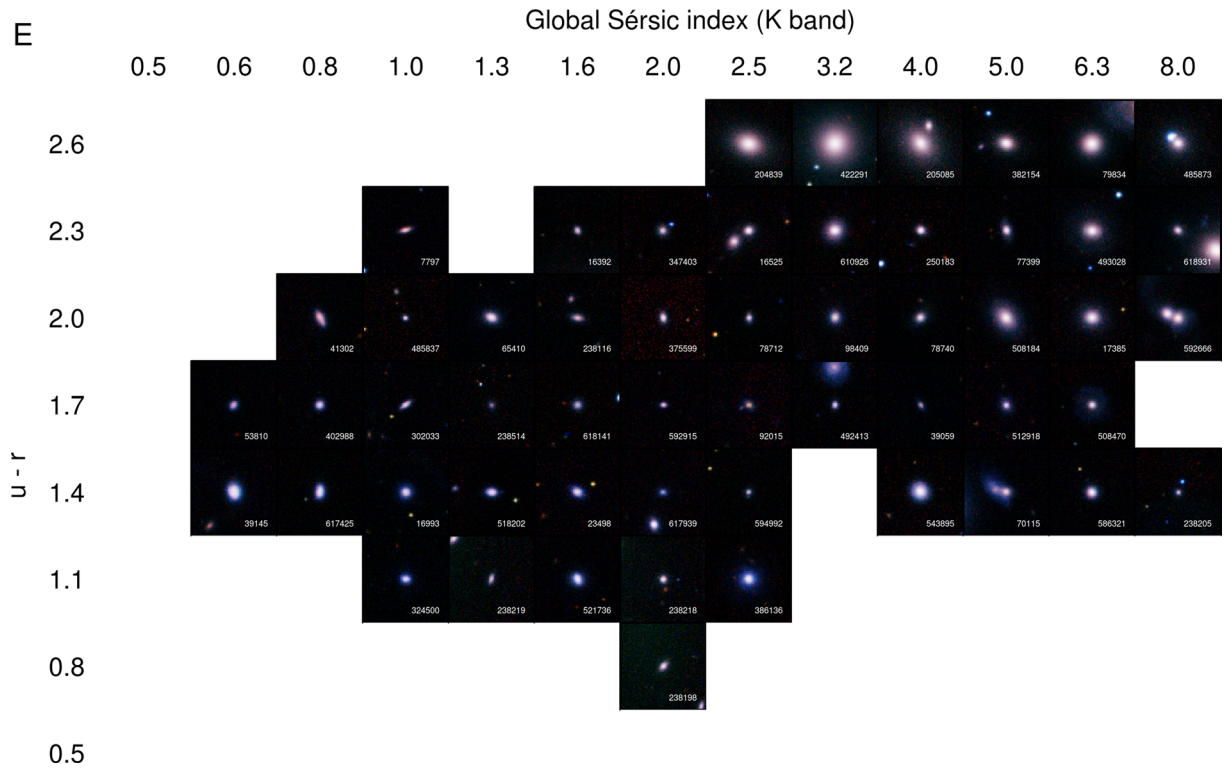

Figure C2. As Fig. C1, but for ellipticals.

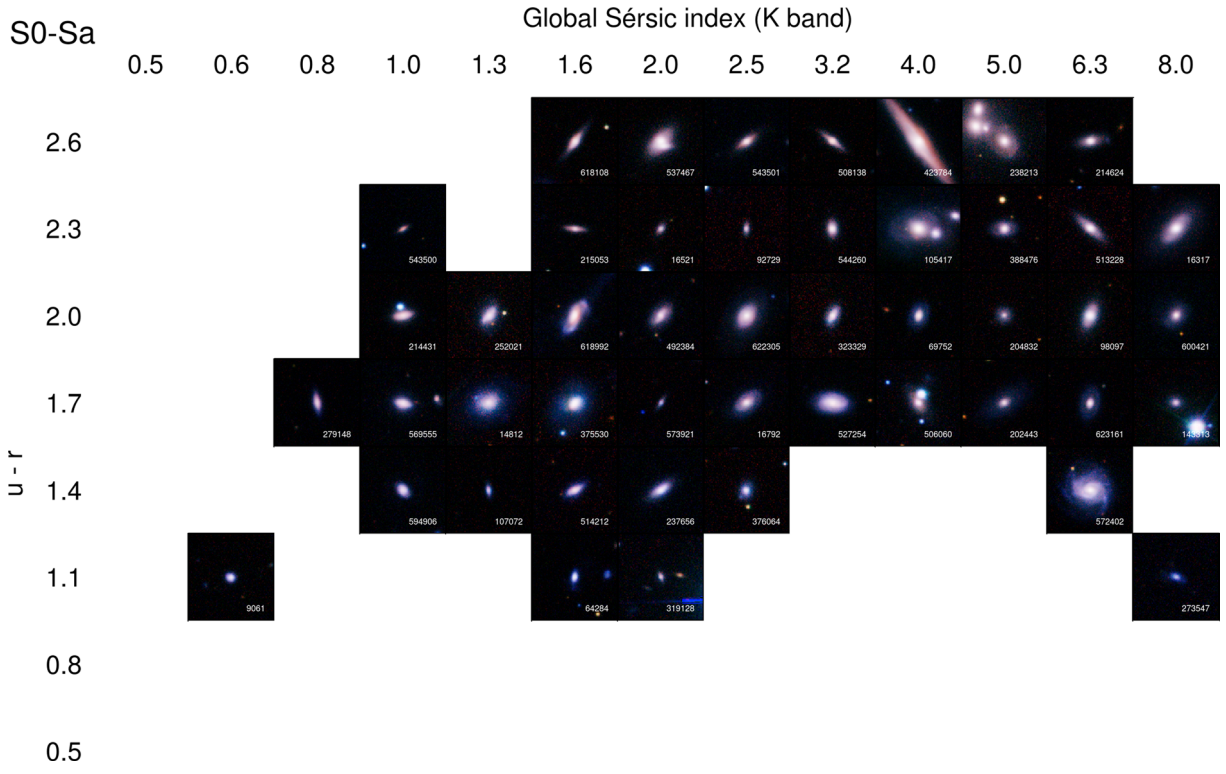

Figure C3. As Fig. C1, but for S0-Sa-type galaxies.

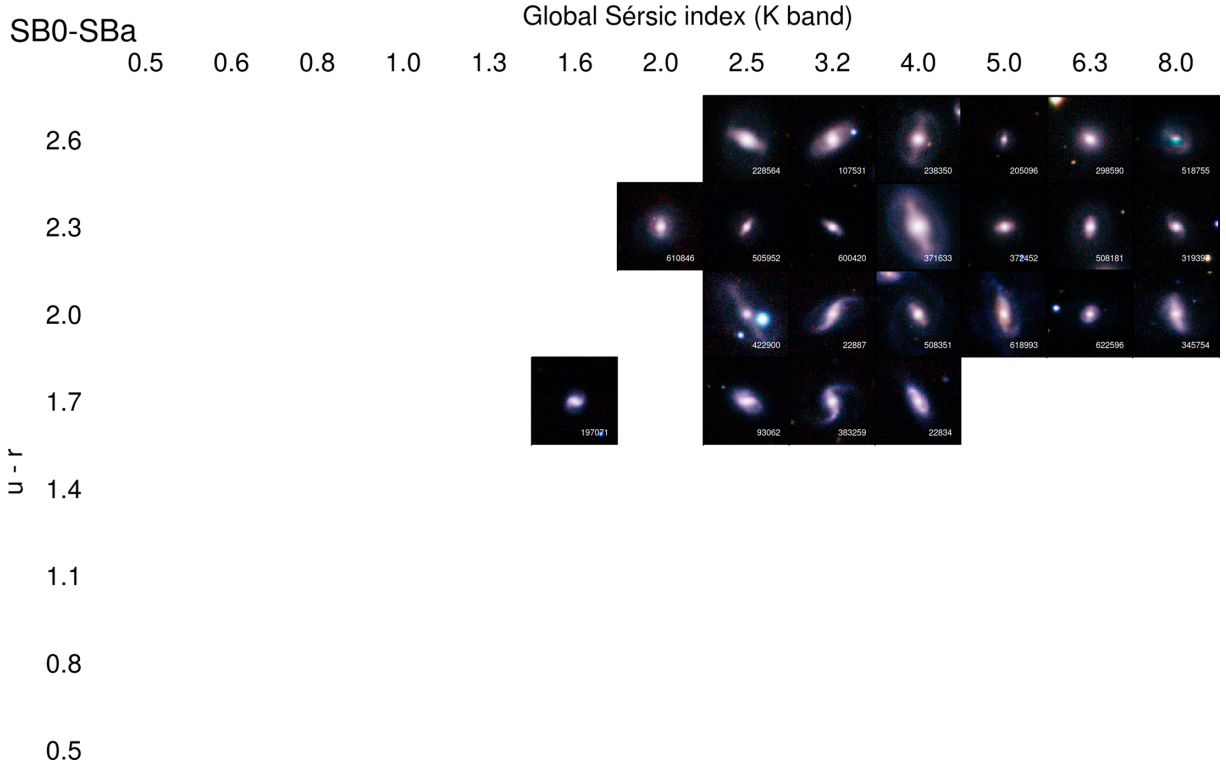

Figure C4. As Fig. C1, but for SB0-SBa-type galaxies.

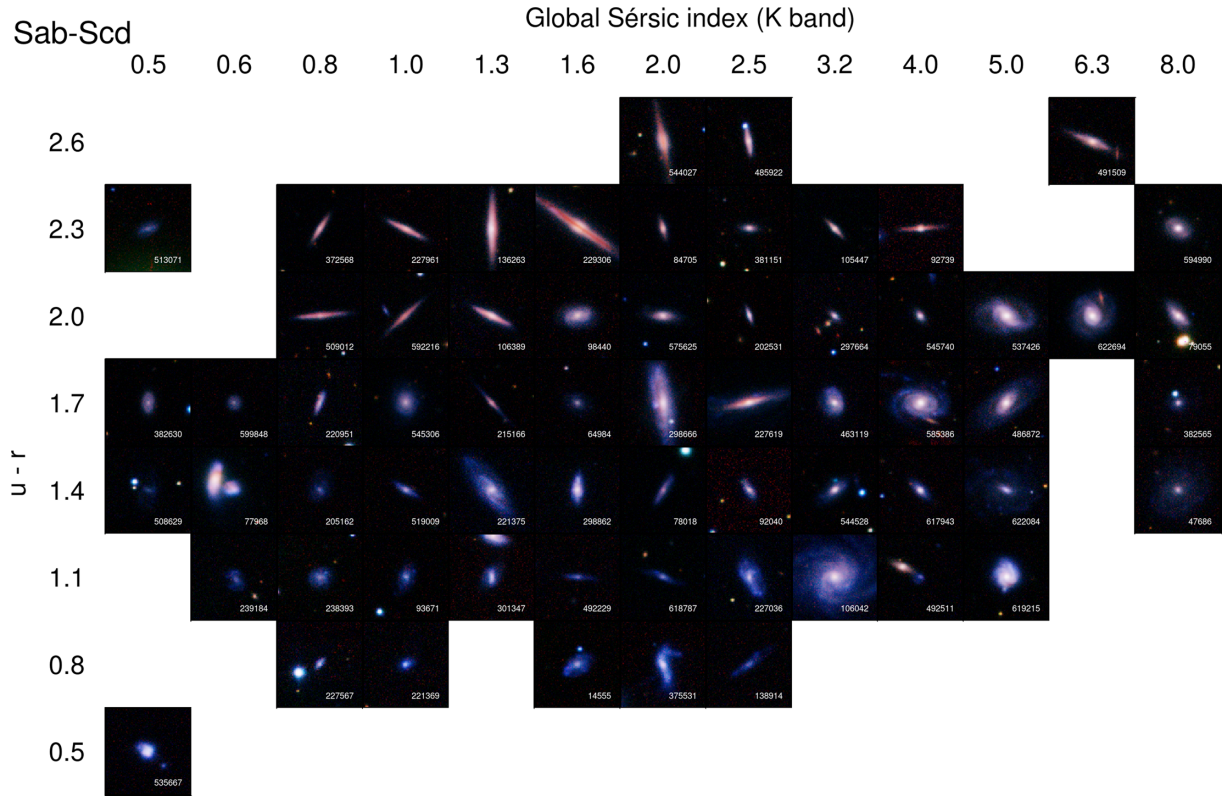

Figure C5. As Fig. C1, but for Sab-Scd-type galaxies.

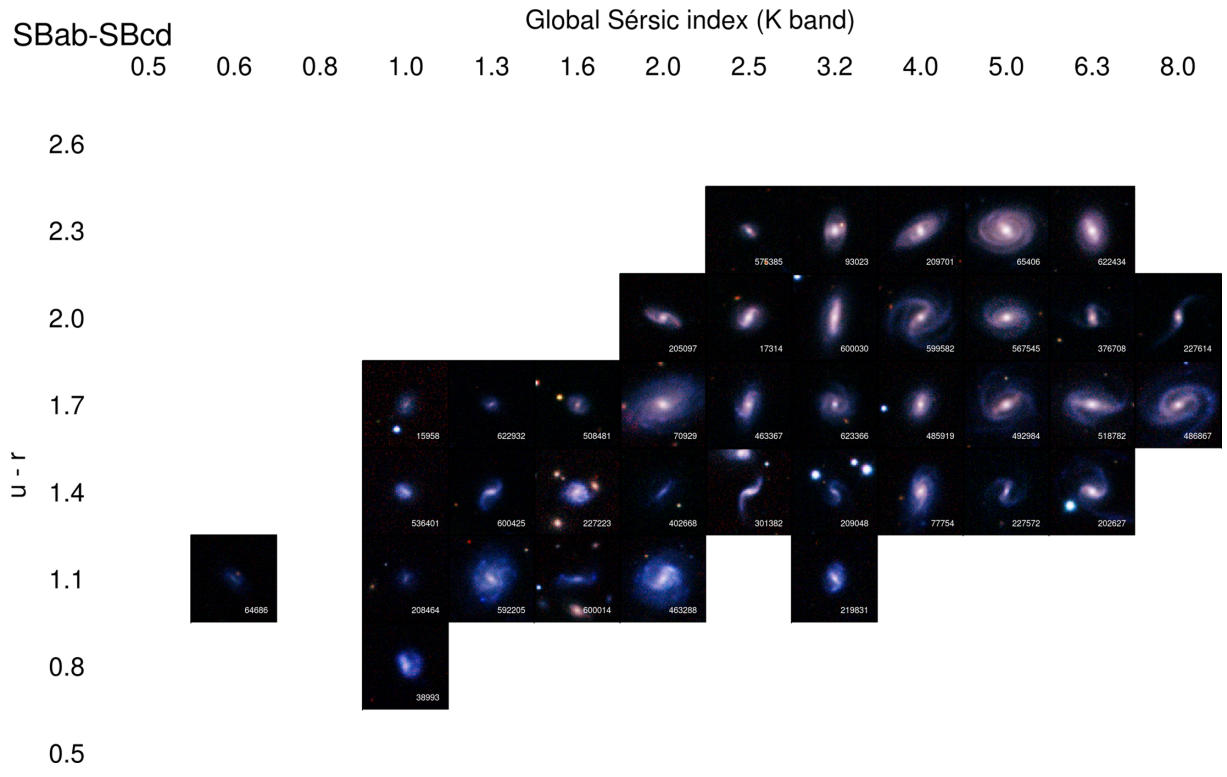

Figure C6. As Fig. C1, but for SBab-SBcd-type galaxies.

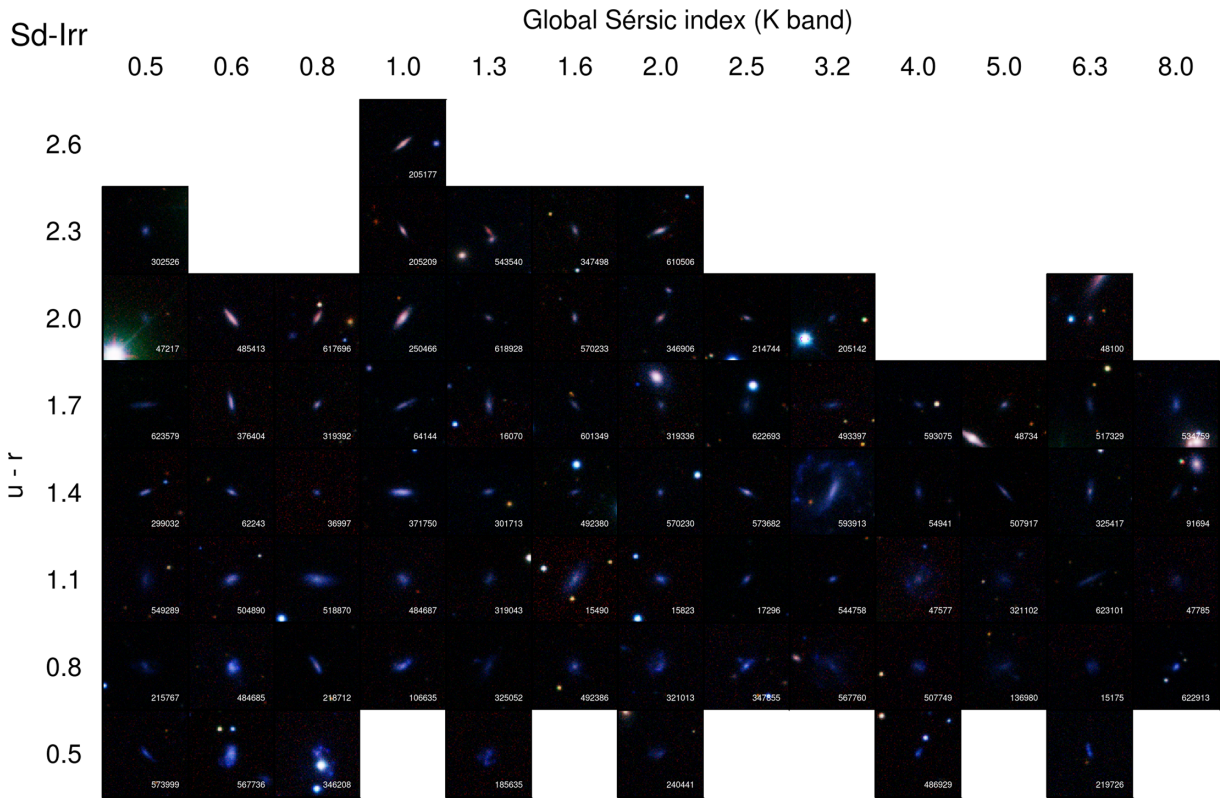

Figure C7. As Fig. C1, but for Sd-Irr-type galaxies.

This paper has been typeset from a TEX/LATEX file prepared by the author.